Pergamon

Int. J. Solids Structures Vol. 35, No. 19, pp. 2429–2455, 1998

0020–7683/98 $19.00 + .00

PII: S0020–7683(97)00144–3

RANDOM FIELD MODELS OF HETEROGENEOUS MATERIALS

M. OSTOJA-STARZEWSKI
Institute of Paper Science and Technology, and Georgia Institute of Technology, 500 10th St., N.W., Atlanta, GA 30318-5794, U.S.A.
E-mail: martin.ostoja@ipst.edu

(*Received* 19 *May* 1997)

Abstract—One of the main challenges in solid mechanics lies in the passage from a heterogeneous microstructure to an approximating continuum model. In many cases (e.g. stochastic finite elements, statistical fracture mechanics), the interest lies in resolution of stress and other dependent fields over scales not infinitely larger than the typical microscale. This may be accomplished with the help of a meso-scale window which becomes the classical representative volume element (RVE) in the infinite limit. It turns out that the material properties at such a mesoscale cannot be uniquely approximated by a random field of stiffness/compliance with locally isotropic realizations, but rather two random continuum fields with locally anisotropic realizations, corresponding, respectively, to essential and natural boundary conditions on the meso-scale, need to be introduced to bound the material response from above and from below. We study the first- and second-order characteristics of these two meso-scale random fields for anti-plane elastic response of random matrix–inclusion composites over a wide range of contrasts and aspect ratios. Special attention is given to the convergence of effective responses obtained from the essential and natural boundary conditions, which sheds light on the minimum size of an RVE. Additionally, the spatial correlation structure of the crack density tensor with the meso-scale moduli is studied. © 1998 Elsevier Science Ltd. All rights reserved.

1. INTRODUCTION

A very wide class of material microstructures displays discontinuities in local properties and thus they are, in principle, piecewise-constant in the sense of a local, pointwise continuum approximation. Examples include polycrystals and composite materials. Consequently, a rational passage from a microstructure to an approximating continuum model is one of the major challenges of contemporary micromechanics. This challenge can be rephrased in terms of two questions:

- What is the size of a classical representative volume element (RVE) of deterministic continuum theories?
- How to set up a stochastic continuum field description below the scale of an RVE?

This paper is devoted to a study of these questions in a very simple setting of anti-plane elasticity, which, by virtue of well-known mathematical analogies relating to the fact that the Laplace equation governs the local behavior, is equivalent to a number of other problems: elastic membrane, thermal conductivity, etc. Typical applications include providing input for stochastic finite element analyses and statistical fracture mechanics.

Regarding the first issue, typical recipes of solid mechanics (Lemaitre and Chaboche, 1994) say that an RVE should be some 10–100 times larger than the size of an inhomogeneity. The need to include lower than the RVE length scale phenomena in elasticity, combined with their non-deterministic character, motivated a number of researchers to work with random fields of stiffness tensors $\mathbf{C} = \{\mathbf{C}(\mathbf{x}, \omega);\ \omega \in \Omega\}$; e.g. (Beran, 1981 Sobczyk, 1985). Implied in such models is the invertibility of the constitutive law, that is

$$\boldsymbol{\varepsilon} = \mathbf{S}(\mathbf{x}, \omega)\boldsymbol{\sigma} \quad \mathbf{S}(\mathbf{x}, \omega) = \mathbf{C}^{-1}(\mathbf{x}, \omega) \tag{1}$$

with $\boldsymbol{\varepsilon}$ and $\boldsymbol{\sigma}$ being uniform fields applied to a hypothetical and unspecified RVE of a random medium. In fact, typically, a locally isotropic form

$$\varepsilon_{ij} = \frac{1}{E}[(1+\nu)\sigma_{ij} - \nu\delta_{ij}\sigma_{kk}] \tag{2}$$

is adopted by simply postulating one or both elastic constants, such as Young's modulus E and Poisson's ratio ν, to be random fields, usually of Gaussian type, with differentiable realizations.

The basic, phenomenological prescription for a conventional RVE postulates the presence of a statistical representation of the microstructure with all the typical microheterogeneities, and thus calls for relatively large volumes. In fact, closely related to this is the concept (Hill, 1963) that the relations between volume average stress and strain should be the same regardless of whether kinematic or stress boundary conditions have been used, that is, when both interpretations of the Hooke's law (1) are fully equivalent. The point is that large volumes of material need to be considered to render the influence of boundary conditions to vanish. An analytical work on the RVE size, using a nonlocal medium formulation, has recently been published by Drugan and Willis (1996). They employ a definition of an RVE as that of *the smallest material volume element of the composite for which the usual spatially constant "overall modulus" macroscopic constitutive representation is a sufficiently accurate model to represent mean constitutive response*. Their conclusion is that very small volumes, on the order of just a few grains, are required.

We consider the issue of size and an RVE from the former standpoint, by employing a formulation of scale-dependent bounds based on finite size test-windows, which were first set up by Huet (1990) and Sab (1992). The idea is to consider the Hooke's law as being either controllable by strains or stresses, and to ask for what window sizes do two responses begin to coincide. This method requires an explicit computational mechanics solution of a number of realizations of possible microstructures, sampled in a Monte-Carlo sense, which in turn allows a determination of statistics of both bounds.

The fact that the *meso-scale window* may be placed anywhere in the material domain, leads to a concept of two approximating random fields (Ostoja-Starzewski, 1993a); we call them *meso-scale random fields*. We investigate the statistics of these random fields as a function of: window size, type of boundary conditions employed in definition of the Hooke's law, mismatch in elastic moduli, and aspect ratio of inclusions. We establish various similarities as well as distinctions between several types of composites: disk–matrix composites with stiff disks vs those with soft disks, composites with soft needle-like inclusions vs ones made of fibers in a matrix of negligible stiffness. Besides the ensemble averages of moduli, we discuss their statistics and spatial correlations.

2. GENERAL CONSIDERATIONS

2.1. *Basic parameters*

In this paper we focus on two-dimensional matrix-inclusion elastic materials in anti-plane shear (Fig. 1). That is, locally the Hooke's law of the matrix (m) and the inclusion (i) is given by

$$\sigma_i = C_{ij}\varepsilon_j \quad i,j = 1,2 \quad C_{ij} = C^{(\mathrm{m})}\delta_{ij} \quad \text{or } C^{(\mathrm{i})}\delta_{ij} \tag{3}$$

where, for simplicity of notation, we denote

$$\sigma_i \equiv \sigma_{i3} \quad \varepsilon_i \equiv \varepsilon_{i3} \quad i,j = 1,2. \tag{4}$$

Parallel to the subscript notation we shall also use the symbolic notation, so that, for example: $C_{ij} \equiv \mathbf{C}$. The governing equation of the piecewise-constant material is

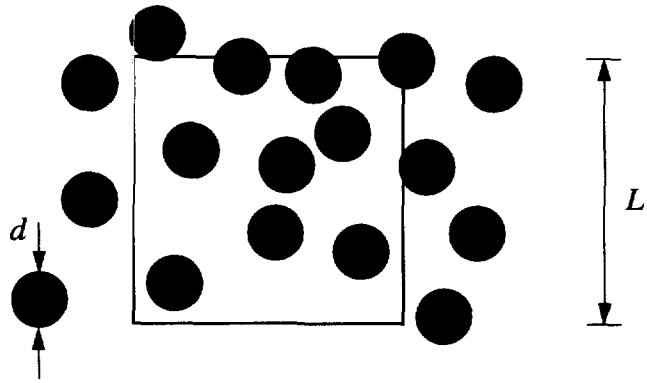

Fig. 1. A realization of random microstructure of a two-phase, disk-matrix composite material, and the window-scale concept. Corresponding scale dependent moduli are shown in Figs 3 and 4.

$$C\left(\frac{\partial^2 u}{\partial x_1^2}+\frac{\partial^2 u}{\partial x_2^2}\right)=0 \quad C=C^{(\mathrm{i})} \quad \text{or } C^{(\mathrm{m})} \quad u\equiv u_3. \tag{5}$$

The isotropy of both stiffness tensors $C^{(\mathrm{m})}$ and $C^{(\mathrm{i})}$ in (3) leads to a so-called *contrast* $C^{(\mathrm{i})}/C^{(\mathrm{m})}$, sometimes called a *mismatch*. It is clear that by increasing the contrast we can go to very stiff inclusions, and approximate a rigid case. Similarly, by decreasing the contrast, we can go to very soft inclusions and reach a system with holes.

While disk is the basic inclusion shape, the departure from this will be of interest. Thus, another basic parameter specifying the composite is the *aspect ratio* of ellipses a/b, where a (b) is the major (minor) semi-axis. By varying the aspect ratio from 1 up through higher values we can model systems having disk-type, ellipse-type, through needle-type inclusions. We are thus led to the concept of a parameter plane as shown in Fig. 2(a).

The third important parameter is the *volume fraction* of inclusions defined by $v^{(\mathrm{i})}=V^{(\mathrm{i})}/V_{\mathrm{total}}$, where the volume V is just an area in a planar system. The range through which $v^{(\mathrm{i})}$ may be varied will depend on the chosen model of placement of circular inclusions in the matrix, in the case of no-overlap condition of inclusions we are limited by a random packing fraction of $\sim 56\%$, while in the case of no such condition, we can go, in principle, up to 100%.

2.2. *Scale-dependent hierarchy of bounds*

Our principal interest is in the determination of the effective stiffness tensor $\mathbf{C}^{\mathrm{eff}}$ of such composite systems over the parameter plane of aspect ratio and contrast, and its correlation to the composite microgeometry. Let us assume that the composite is made of just one size, d, of inclusions, and fractal geometries are excluded. In principle, any sample of a composite, such as the one shown in Fig. 1, is disordered. It is, basically, a deterministic realization $\mathbf{B}(\omega)$ of a random medium $\mathbf{B}=\{\mathbf{B}(\omega);\omega\in\Omega\}$. In order to define effective properties of the material at a point $\mathbf{x}$, we place a *window* of size L centered at that point. Windows of size $L=0$ yield the pointwise limit of local properties, while windows of finite size define a scale over which some "smearing out" is conducted. In the following we shall study this smearing out as a function of a nondimensional window scale

$$\delta=\frac{L}{d}. \tag{6}$$

It is immediately clear that $\delta\to\infty$ should result in a conventional continuum limit typically sought in the effective medium theories. However, when considering finite δ values, the response is not deterministic, so that the window represents a statistical volume element (SVE). In order to determine its response, two types of boundary conditions will be employed:

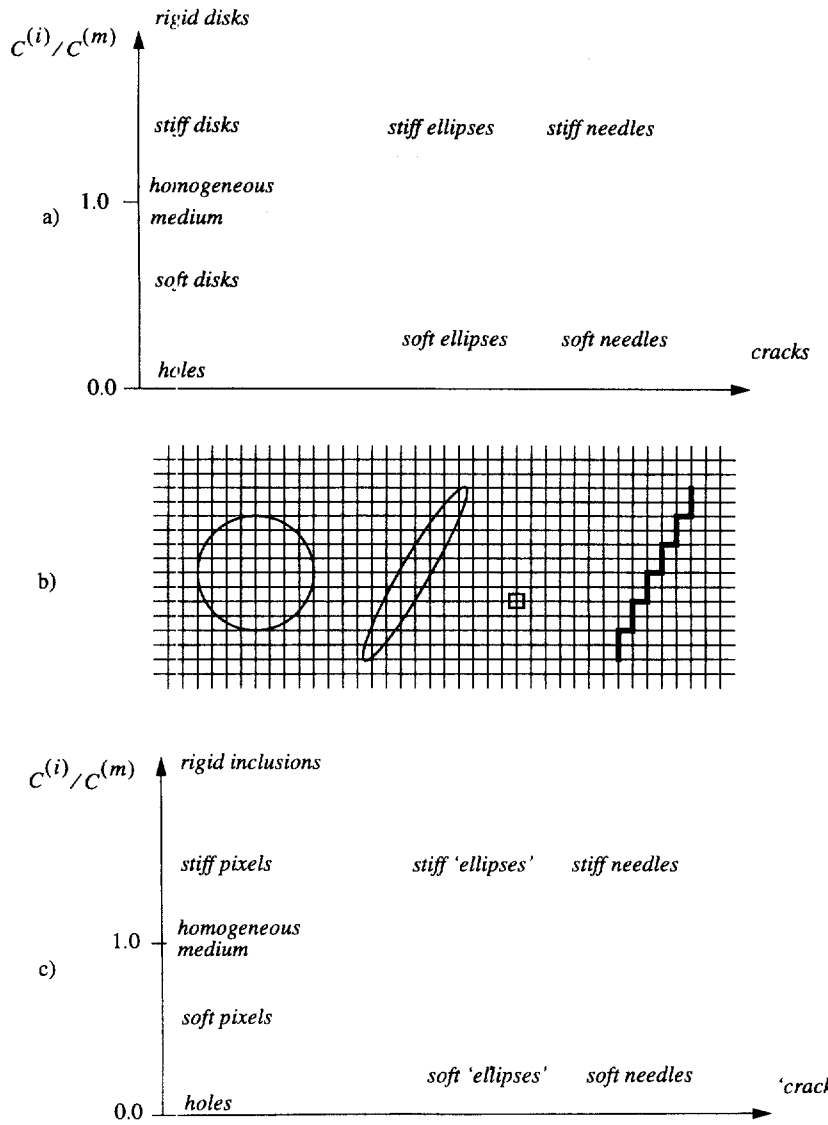

Fig. 2. (a) A parameter plane: aspect ratio of inclusions and the contrast; (b) spring network as a basis for resolution of round disks, ellipses, pixels, and needles in the parameter plane; (c) another interpretation of the parameter plane: from pixels to needles.

(a) *Essential* (Dirichlet, displacement-controlled)

$$u = \bar{\varepsilon}_i x_i \tag{7}$$

which yield a tensor $\mathbf{C}_\delta^e$ ("e" stands for essential boundary conditions), where u is the displacement, $\bar{\varepsilon}$ is the volume (area) average strain, and $\mathbf{x}$ is a position vector.

(b) *Natural* (Neumann, or stress-controlled):

$$t = \bar{\sigma}_i n_i \tag{8}$$

which yield the tensor $\mathbf{C}_\delta^n = (\mathbf{S}_\delta^n)^{-1}$ ("n" stands for natural boundary conditions), where t is the stress traction, $\bar{\sigma}$ is the volume (area) average stress, and $\mathbf{n}$ is the outer unit normal to the window's boundary. In the above we employ boldface for a second-rank tensor, and an overbar for a spatial average over the window domain. Note that the formulation via

the condition (7) corresponds to an interpretation of the effective Hooke's law from the standpoint of controllable strains

$$\sigma_i = C_{ij}\bar{\varepsilon}_j \quad \mathbf{C} = \mathbf{C}^{\mathrm{e}}_{\delta} \tag{9}$$

while the formulation via the condition (8) corresponds to an interpretation of the effective Hooke's law from the standpoint of controllable stresses

$$\varepsilon_i = S_{ij}\bar{\sigma}_j \quad \mathbf{S} = \mathbf{S}^{n}_{\delta}. \tag{10}$$

We observe that $\mathbf{C}^{\mathrm{e}}_{\delta}$ is, in general, different from $\mathbf{C}^{n}_{\delta}$ as it provides an *upper estimate* on the effective stiffness of the given specimen, while the latter represents a *lower estimate*. In fact, it can be shown from the variational principles of mechanics, that the effective macroscopic stiffness tensor $\mathbf{C}^{\mathrm{eff}}$ is bounded by two tensors $\langle \mathbf{C}^{\mathrm{e}}_{\delta} \rangle$ and $\langle \mathbf{S}^{n}_{\delta} \rangle^{-1}$, where $\langle\ \rangle$ denotes the ensemble averaging, i.e. averaging over the space of all realizations Ω. As the scale δ approaches its continuum limit $\delta \to \infty$ we get ever tighter bounds on the effective stiffness $\mathbf{C}^{\mathrm{eff}}$, this is expressed by a hierarchy of δ-dependent bounds

$$\mathbf{C}^{\mathrm{R}} \equiv (\mathbf{S}^{\mathrm{R}})^{-1} \equiv \langle \mathbf{S}^{n}_{1} \rangle^{-1} \leqslant \langle \mathbf{S}^{n}_{\delta'} \rangle^{-1} \leqslant \langle \mathbf{S}^{n}_{\delta} \rangle^{-1} \leqslant \mathbf{C}^{\mathrm{eff}} \leqslant \langle \mathbf{C}^{\mathrm{e}}_{\delta} \rangle \leqslant \langle \mathbf{C}^{\mathrm{e}}_{\delta'} \rangle \leqslant \langle \mathbf{C}^{\mathrm{e}}_{1} \rangle \equiv \mathbf{C}^{\mathrm{V}} \quad \forall \delta' < \delta. \tag{11}$$

In eqn (11) $\mathbf{C}'$ and $\mathbf{C}''$ denote the Voigt and Reuss bounds, corresponding to windows at the smallest scale ($\delta = 1$). In other words, the effective response depends on the boundary conditions, and the influence of the latter disappears as the sample becomes infinite. The order relation employed in (11) means that $t \cdot \mathbf{B} \cdot t \leqslant t \cdot \mathbf{A} \cdot t$ for any vector $t \neq 0$ and two second rank tensors $\mathbf{A}$ and $\mathbf{B}$. In the special case of the microstructure being characterized by an isotropic statistics, $\mathbf{C}^{\mathrm{eff}}$ is isotropic, i.e. $\mathbf{C}^{\mathrm{eff}} = \mathbf{I}C^{\mathrm{eff}}$ where $\mathbf{I}$ is the identity tensor.

The hierarchy (11) was first derived by Huet (1990) [see also Huet (1992, 1994)]. A more rigorous proof using techniques of homogenization and probability theories was given by Sab (1992); he also showed that a weak mixing, rather than just ergodic, property of random fields is required. The decrease of the upper bound with increasing scale appears to have first been demonstrated through a computational mechanics study of planar random triangular networks of Delaunay topology by Ostoja-Starzewski and Wang (1989). The subject of determination of the hierarchy (11) for several types of composites has been pursued in (Ostoja-Starzewski, 1994) and (Ostoja-Starzewski and Schulte, 1996). It is also important to note that mixed boundary conditions result, at any scale δ, in a response bounded by (11) (Hazanov and Huet, 1994).

The derivation of a right-hand side sequence of inequalities in (11) rests on an observation, following from a variational principle, that the effective moduli of a given domain of a heterogeneous material under (7) are lower than the effective moduli of any partition of the same domain subjected to (7) on its entire boundary. The same type of argument is employed, together with condition (8) and a minimum complementary potential energy principle, to prove the left-hand side sequence of inequalities in (11). By proceeding in a similar manner we can state the following inequalities between higher-order ($m \geqslant 2$) moments of moduli obtained from (7)

$$0 \leqslant (\mathbf{C}^{\mathrm{eff}})^{m} \leqslant \langle (\mathbf{C}^{\mathrm{e}}_{\delta})^{m} \rangle \leqslant \langle (\mathbf{C}^{\mathrm{e}}_{\delta'})^{m} \rangle \leqslant \langle (\mathbf{C}^{\mathrm{e}}_{1})^{m} \rangle \quad \forall \delta' < \delta \tag{12}$$

and from (8)

$$0 \leqslant (\mathbf{S}^{\mathrm{eff}})^{m} \leqslant \langle (\mathbf{S}^{n}_{\delta})^{m} \rangle \leqslant \langle (\mathbf{S}^{n}_{\delta'})^{m} \rangle \leqslant \langle (\mathbf{S}^{n}_{1})^{m} \rangle \quad \forall \delta' < \delta \tag{13}$$

which say that the noise is strongest on the microscale; it is absent in the $\delta \to \infty$ limit.

These results were first given, without proof, in (Ostoja-Starzewski, 1993a). To prove (12), let us introduce a partition of a square-shaped window $B_\delta(\omega)$, of volume V_δ, into four smaller square-shaped windows $B^s_{\delta'}(\omega)$, $s = 1, \ldots, 4$, of size $\delta' = \delta/2$ and volume $V_{\delta'}$ each. Next, we introduce a restricted version of the essential boundary condition (7) in the sense that it applies to all the boundaries of all four $B^s_{\delta'}(\omega)$ rather than just to $B_\delta(\omega)$. Now, observe that the minimum potential energy principle implies that the strain energy $U^r(\omega)$ stored in the body $B_\delta(\omega) = \bigcup_{s=1}^4 B^s_{\delta'}(\omega)$ under this restricted boundary condition bounds the energy $U(\omega)$ stored in the same body under the condition (7)

$$\frac{1}{2} V_\delta \bar{\varepsilon} \cdot \mathbf{C}^e_\delta \cdot \bar{\varepsilon} = U(\omega) \leqslant U^r(\omega) = \sum_{s=1}^4 \frac{1}{2} V_{\delta'} \bar{\varepsilon} \cdot \mathbf{C}^{e,s}_{\delta'} \cdot \bar{\varepsilon}. \tag{14}$$

The superscript "r" indicates a restriction. Here $\mathbf{C}^e_\delta$ and $\mathbf{C}^{e,s}_{\delta'}$ are the effective tensors of $B_\delta(\omega)$ and $B^s_{\delta'}(\omega)$, respectively. If we now consider the test $\bar{\varepsilon} \equiv (\bar{\varepsilon}_1, 0)$, we find from (14) that

$$\left(\frac{1}{2} V_\delta \bar{\varepsilon} \cdot \mathbf{C}^e_\delta \cdot \bar{\varepsilon}\right)^2 \leqslant \left(\sum_{s=1}^4 \frac{1}{2} V_{\delta'} \bar{\varepsilon} \cdot \mathbf{C}^{e,s}_{\delta'} \cdot \bar{\varepsilon}\right)^2 \quad C^e_\delta \equiv C_{11} \quad \bar{\varepsilon} \equiv (\bar{\varepsilon}_1, 0). \tag{15}$$

Upon carrying out ensemble averaging and noting spatial homogeneity and ergodicity of $\mathbf{B}$, as well as $V_\delta = 4V_{\delta'}$, we obtain

$$\langle (C^e_\delta)^2 \rangle \leqslant \langle (C^e_{\delta'})^2 \rangle. \tag{16}$$

Proceeding in this fashion for the $\bar{\varepsilon} \equiv (0, \bar{\varepsilon}_2)$ and $\bar{\varepsilon} \equiv (\bar{\varepsilon}_1, \bar{\varepsilon}_2)$ tests, we find the same inequalities for C_{12} and C_{22} components of $\mathbf{C}^e_\delta$, which leads us to (12).

In order to prove (13) we can introduce a restricted version of the natural boundary condition (8) in the sense that $t^r = \bar{\sigma}_{ij} n_j$ applies to all the boundaries of all four $B^s_{\delta'}(\omega)$. Next, it follows from the minimum complementary potential energy principle, that the complementary potential energy $U^{*r}(\omega)$ stored in the body $B_\delta(\omega) = \bigcup_{s=1}^4 B^s_{\delta'}(\omega)$ under condition (8) bounds the complementary potential energy $U^*(\omega)$ stored in the same body under (8)

$$\frac{1}{2} V_\delta \mathbf{q} \cdot \mathbf{S}^n_\delta \cdot \mathbf{q} = \mathbf{\Phi}^*(\omega) \leqslant \mathbf{\Phi}^{*r}(\omega) = \sum_{s=1}^4 \frac{1}{2} V_{\delta'} \mathbf{q} \cdot \mathbf{S}^{n,s}_{\delta'} \cdot \mathbf{q}. \tag{17}$$

Here $\mathbf{S}^n_\delta$ and $\mathbf{S}^{n,s}_{\delta'}$ are the effective compliance tensors of $B_\delta(\omega)$ and $B^s_{\delta'}(\omega)$, respectively. Also here we can take the second powers when considering the test $\bar{\sigma} \equiv (\bar{\sigma}_1, 0)$ to get

$$\left(\frac{1}{2} V_\delta \sigma \cdot \mathbf{S}^n_\delta \cdot \sigma\right)^2 \leqslant \left(\sum_{s=1}^4 \frac{1}{2} V_{\delta'} \bar{\sigma} \cdot \mathbf{S}^{n,s}_{\delta'} \cdot \bar{\sigma}\right)^2 \quad S^e_\delta \equiv S_{11} \quad \bar{\sigma} \equiv (\bar{\sigma}_1, 0). \tag{18}$$

From this, upon ensemble averaging, we find

$$\langle (S^n_\delta)^2 \rangle \leqslant \langle (S^n_{\delta'})^2 \rangle \tag{19}$$

and by induction combined with the other two tests, the hierarchy (13) can be deduced.

2.3. *Numerical solution method*

In order to solve the field equations of a two-phase composite we employ a spring network method, Fig. 2(b). The idea is to approximate the planar, piecewise-constant continuum by a very fine mesh. In the following, we shall assume that a square mesh for discretization of the displacement field u is used. The governing equations are thus

$$u(i,j)[k_r+k_l+k_u+k_d]-u(i+1,j)k_r-u(i-1,j)k_l-u(i,j+1)k_u-u(i,j-1)k_d=0. \quad (20)$$

Here i and j are the coordinates of mesh points, and k_e, k_l, k_u and k_d are defined from the series spring model

$$\begin{aligned} k_r &= [1/C(i,j)+1/C(i+1,j)]^{-1} \\ k_l &= [1/C(i,j)+1/C(i-1,j)]^{-1} \\ k_u &= [1/C(i,j)+1/C(i,j+1)]^{-1} \\ k_d &= [1/C(i,j)+1/C(i,j-1)]^{-1} \end{aligned} \quad (21)$$

where $C(i,j)$ is the property at a point (i,j). It is seen that this type of a discretization can equivalently be called a finite difference model. However, in the case of in-plane elasticity problems, a spring network approach is not identical to a finite difference method. As explained, for example, in (Ostoja-Starzewski *et al.*, 1996) the node–node connections of a spring network do really have a meaning of springs, whereas the finite difference connections do not.

Resolution of several different types of inclusions by a spring network is shown in Fig. 2(b). That is, we can model disks, ellipses and needles. Admittedly, this type of modeling is approximate, so that a somewhat different interpretation of a parameter plane is given in Fig. 2(c). It is seen that disks may most simply be modeled as single pixels or more accurately as finite regions; in the latter case arbitrary anisotropies can be modeled. The former case allows one to deal with very large scale systems, while the latter allows a much better resolution of local stress/strain fields within and around the inclusions. By decreasing the spring network mesh size, an increasingly better accuracy can be achieved. Somewhat more accurate results may be obtained by a finite element model, albeit at a higher price of costly and cumbersome remeshing for each and every new disk configuration $\mathbf{B}(\omega)$ which is required in statistical studies.

It is noteworthy that, in contradistinction to a finite element method, no need for remeshing and constructing of a stiffness matrix exists in our spring network method: spring constants are very easily assigned throughout the mesh, and the conjugate gradient method finds the solution of the equilibrium displacement field $u(i,j)$. In that manner, a system having a million degrees-of-freedom (1000×1000 nodes) can readily be handled in a matter of a few hours on a computer work-station with $\sim$90 MB of random access memory. For 2000×2000 nodes one requires some 360 MB, and so on, because of a linear scaling of memory requirements with the number of degrees-of-freedom. We sometimes employ two other methods beside the conjugate gradient: an overrelaxation method, and linear algebraic solvers. Additionally, in some counterintuitive cases (e.g. low contrast in Section 3, we check the results of the essential (e) and natural (n) boundary value problems via the Betti's reciprocity theorem

$$\int_S u_i^{(n)} t_i^{(e)}\,\mathrm{d}S = \int_S u_i^{(e)} t_i^{(n)}\,\mathrm{d}S \quad S=\partial B. \quad (22)$$

The quality of approximation of ellipses and needle-type cracks/inclusions can be varied according to the number of nodes chosen to represent such objects. Local fields cannot be perfectly resolved, but the solution by the spring network is sufficient to rapidly establish the elastic moduli of a number of different $\mathbf{B}(\omega)$ realizations from the random medium $\mathbf{B}$, and the corresponding statistics with good accuracy.

3. DISK–MATRIX COMPOSITES

3.1. *Generation via a Poisson point process*

In order to generate a field of round disks, we employ a *Poisson point process* subject to a *sequential inhibition* rule: throw Poisson points on a plane and keep only those which

fall no closer than d_{min} to any previous ones. Note that $d_{min} = 2r$ permits the touching of disks, a situation we prevent by setting $d_{min} = 1.1 \cdot 2r$, so as to avoid the numerically and analytically difficult problem of very narrow necks between disks. This is also called a *random sequential addition* process (Torquato, 1991). Strictly speaking, the Poisson point process of intensity λ as specified by ($|A|$ is a Lebsegue measure of the set A)

$$P\{N(A) = k\} = e^{-\lambda|A|}\frac{\lambda|A|}{k!} \quad A \subset \mathbf{R}^2 \tag{23}$$

occurs on the entire $\mathbf{R}^2$ plane, and so, its numerical simulation must necessarily be done on a compact subset, which actually involves a binomial point process (Stoyan *et al.*, 1987). Note that the classical "car-parking problem" is a simple sequential inhibition process in one dimension. Also note that a variety of other processes can be employed to achieve other disk packings.

3.2. *Hierarchy of bounds and statistics*

The hierarchy of bounds (11) is now illustrated on two examples of a disk–matrix composite at $v^{(i)} = 20\%$: one with relatively soft and another with relatively hard inclusions. In the first case we have a soft matrix ($C^{(m)} = 1.0$) and consider $C^{(i)} = 10^2$ in Fig. 3(a), and

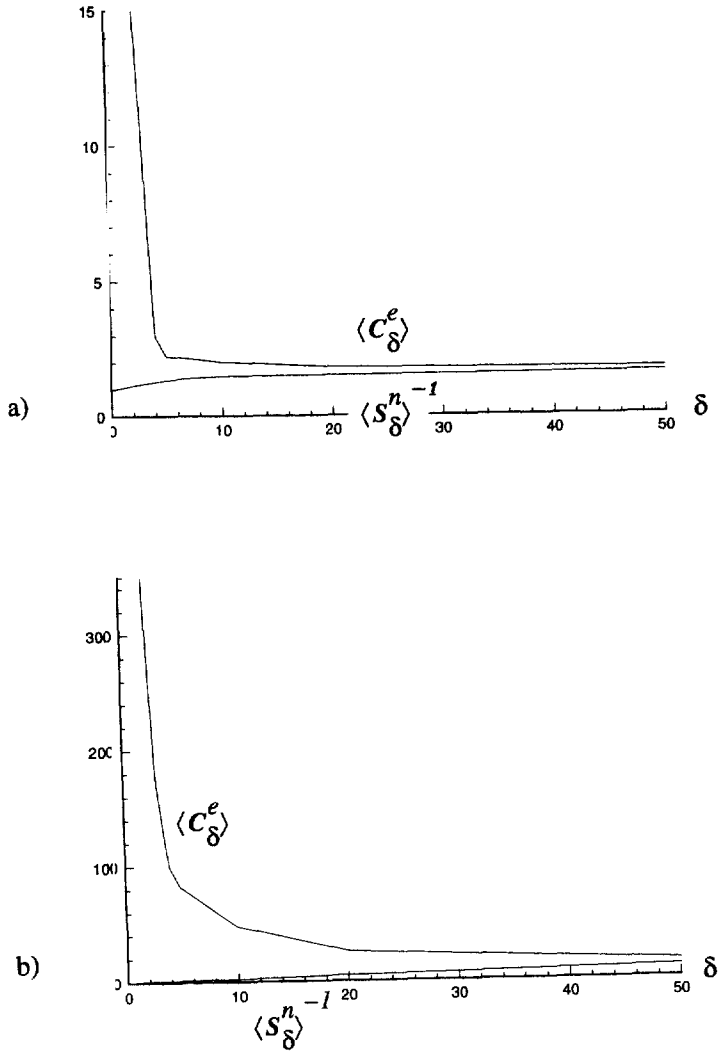

Fig. 3. A hierarchy of scale dependent bounds of stiffnesses of the disk–matrix composite of Fig. 1 at contrasts 100 (a), and 10^4 (b). In both cases $C^{(m)} = 1$, $C^{(i)} = 100$ in (a), $C^{(i)} = 10^4$ in (b).

$C^{(i)} = 10^4$ in Fig. 3(b). Both plots were obtained by using a spring network with 10 bonds per diameter of a single disk, and by conducting computations at windows from $\delta = 2$–50; the latter scale corresponds to windows having 500×500 nodes. For very small windows as many as 100 samples $\mathbf{B}(\omega)$ were run, whereas at the largest scales just a few realizations were needed to obtain the averages. Note that the second case [Fig. 3(b)] corresponds to the top of the parameter plane at the aspect ratio 1 in Fig. 2(a). Clearly, as the contrast in the composite increases, the bounds take larger window scales to converge. It is seen that in order to attain a 10%, difference between $\langle \mathbf{C}_\delta^e \rangle$ and $\langle \mathbf{S}_\delta^n \rangle^{-1}$, one has to take windows that are some 10 and 50 times larger than a single inclusion, for these two contrasts, respectively.

In Fig. 4 we show results for the opposite case: soft inclusions in a hard matrix, with the same volume fraction $v^{(i)} = 20\%$; the same mesh resolution as before is employed here. Again, we consider two cases of contrast, $C^{(i)} = 10^{-2}$ and 10^{-4}, while keeping the matrix at $C^{(m)} = 1.0$. The first one is shown in Fig. 4(a), the second one in Fig. 4(b), and both were obtained with exactly the same spring network resolution as above. As before, an increase in the contrast in the composite has the effect of slowing down the convergence of $\langle \mathbf{C}_\delta^e \rangle$ and $\langle \mathbf{S}_\delta^n \rangle^{-1}$ with δ, but, by comparison with Fig. 3, this convergence is relatively much slower for low contrasts. It follows that one needs to go to very large scales in order to homogenize such a composite material. This is the principal difference from the case of low contrasts.

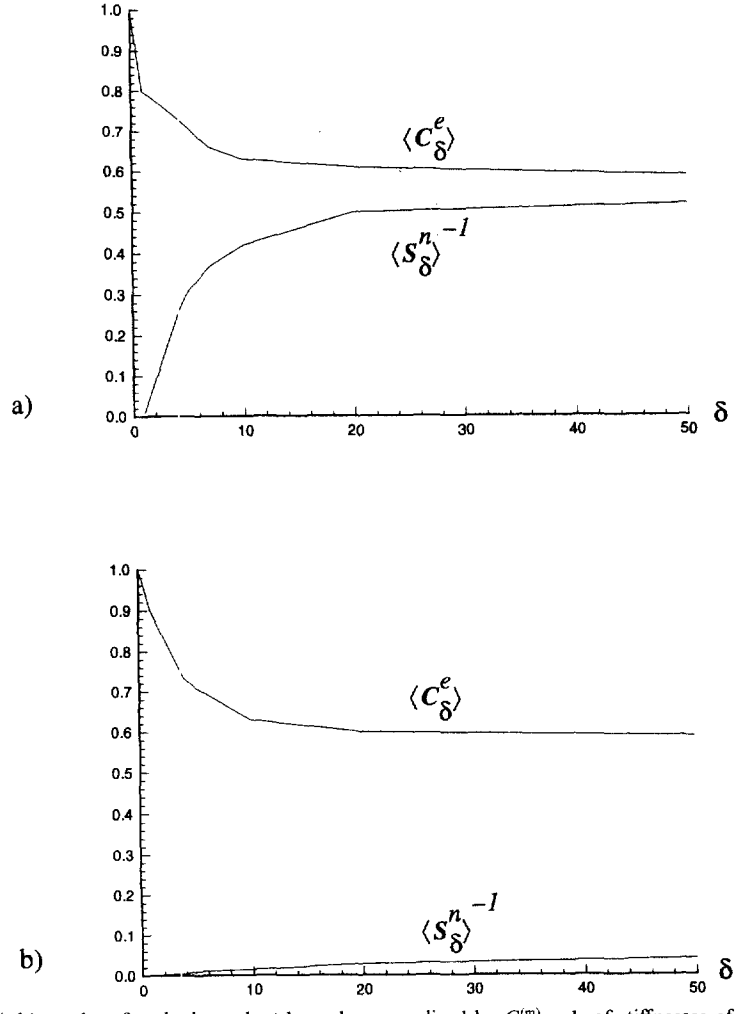

Fig. 4. A hierarchy of scale dependent bounds, normalized by $C^{(m)} = 1$, of stiffnesses of the disk-matrix composite of Fig. 1 at contrasts 10^{-2} (a), and 10^{-4} (b).

4. RANDOM FIELD MODELS

4.1. *Scale dependence via beta distribution*

As discussed earlier, a random medium $\mathbf{B}$ is a set of deterministic media $\mathbf{B}(\omega)$, i.e. $\mathbf{B} = \{\mathbf{B}(\omega); \omega \in \Omega\}$. A basic description of a two-phase microstructure is given in terms of an indicator function

$$f_m(\mathbf{x}, \omega) \to \begin{cases} 1 & \text{if } \mathbf{x} \in \mathbf{B}_m \\ 0 & \text{if } \mathbf{x} \in \mathbf{B}_i \end{cases} \tag{24}$$

where $\mathbf{B}_m(\omega)$ and $\mathbf{B}_i(\omega)$ are the portions of the body occupied by phases m and i, respectively. Various relations are known to hold for the moments of $f_m(\mathbf{x}, \omega)$ [see Beran (1968); Willis (1983); Torquato (1991)], but in the following we need the elementary fact

$$v^{(m)} = \langle f_m \rangle \quad v^{(i)} = 1 - v^{(m)}. \tag{25}$$

One role of the indicator function is that it gives the local property at any point

$$C(\mathbf{x}, \omega) = f_m(\mathbf{x}, \omega) C^{(m)} + [1 - f_m(\mathbf{x}, \omega)] C^{(i)}. \tag{26}$$

Recalling our definition of δ, we see that this is a pointwise limit $\delta = \delta_0 = 0$, which is described by a probability density of $C(\mathbf{x}, \omega)$

$$p(C(\mathbf{x})) = v^{(m)} \delta(C(\mathbf{x}) - C^{(m)}) + v^{(i)} \delta(C(\mathbf{x}) - C^{(i)}). \tag{27}$$

The Dirac deltas on the right are weighted by the volume fractions of phases m and i, respectively.

Suppose now that we sample the local properties not in this pointwise limit, but rather at some finite $0 < \delta_1 < 1$, that is smaller than the inclusion size. Figure 5 shows that if we take a finite size window, it can fall in either of two phases, or on the boundary of inclusions. The former possibility of the pointwise limit, considered in the preceding paragraph, corresponded to a Lebesgue measure zero and thus we simply had eqn (27). This discrete distribution is now replaced by a continuous one such as shown by the curve p_1. Note that the probability mass is distributed continuously between $C^{(m)}$ and $C^{(i)}$, but not outside this finite range.

As we increase the window size, the concentration of the probability mass flows away from the end points of the interval. Considering a window larger than the inclusion size ($\delta > 1$), we note a redistribution, or flow, of the probability mass away from the end points of the interval $[C^{(m)}, C^{(i)}]$ towards some region as indicated by the curve p_2. As $\delta \to \infty$, $p\{C_\delta\}$ tends to a causal distribution centered at $C^{\text{eff}} \equiv C_\infty$—graph p_∞.

These considerations indicate that of all the classical probability densities, *beta* is the most convenient one to describe this scale effect while keeping all admissible values within a finite range. It is given by

$$p(C, a, b, C^{(m)}, C^{(i)}) = \frac{C^{a-1}(1-C)^{b-1}}{(C^{(i)} - C^{(m)}) B(a, b)} \quad \text{for } C^{(m)} < C < C^{(i)} \tag{28}$$

where

$$B(a, b) = \frac{\Gamma(a+b)}{\Gamma(a)\Gamma(b)} \tag{29}$$

with Γ being the gamma function. Another advantage of beta is the fact that it depends on four, rather than three or just two, parameters as is often the case with other classical distributions; these parameters are a, b, $C^{(m)}$, $C^{(i)}$.

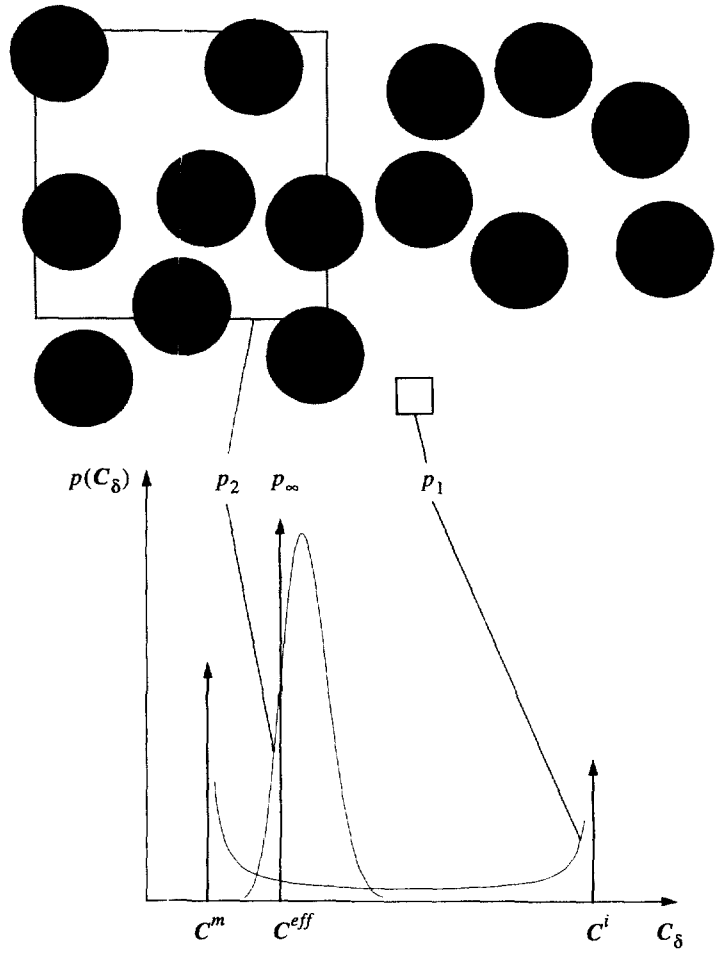

Fig. 5. Sampling of the meso-scale property (trace of C_δ) of a disk–matrix composite via windows of different sizes. The beta distribution gives a practical approximation for the entire range of window sizes, showing four cases: the pointwise limit of eqn (27), the scale δ_1 and fit p_1, the scale δ_2 and fit p_2, and the scale $\delta \to \infty$ and the causal distribution p_∞.

Strictly speaking, we have so far justified the beta distribution as a good fit for the trace C_{ii} of C_{ij}, and a question still remains as to the other features of this effective stiffness tensor. In the following we shall focus on $C_{12,\max}$, which certainly is the same as the radius of the Mohr's circle of a given C_{ij} tensor

$$C_{12,\max} = R = \sqrt{(C_{11}-C_{22})^2/4+C_{12}^2}. \tag{30}$$

In Fig. 6 we display the probability densities of $\mathbf{C}_\delta^e|_{\delta=10}$ of the disk–matrix composite considered earlier in Fig. 3(a). That is in Fig. 6(a) we show $C_{ii}/2$ and in Fig. 6(b) we show $C_{12,\max}$. The first of these confirms the beta character of the trace, while the second one indicates that the radius of the Mohr's circle is strongly positively skewed. It is interesting to compare these results with those for compliances $\mathbf{S}_\delta^e|_{\delta=10}$ obtained from natural boundary conditions, see Fig. 7(a) and (b) which shows $S_{ii}/2$ and in Fig. 6(b) we show $S_{12,\max}$. We observe that while the densities of traces are similar, the skewness of $p(S_{12,\max})$ is weaker than that of $p(\mathbf{C}_{12,\max})$; we return to this issue in Section 5.

4.2. *From discrete to continuum random fields*

It is clear from eqn (24) that the indicator function (in two dimensions) is a random field

a)

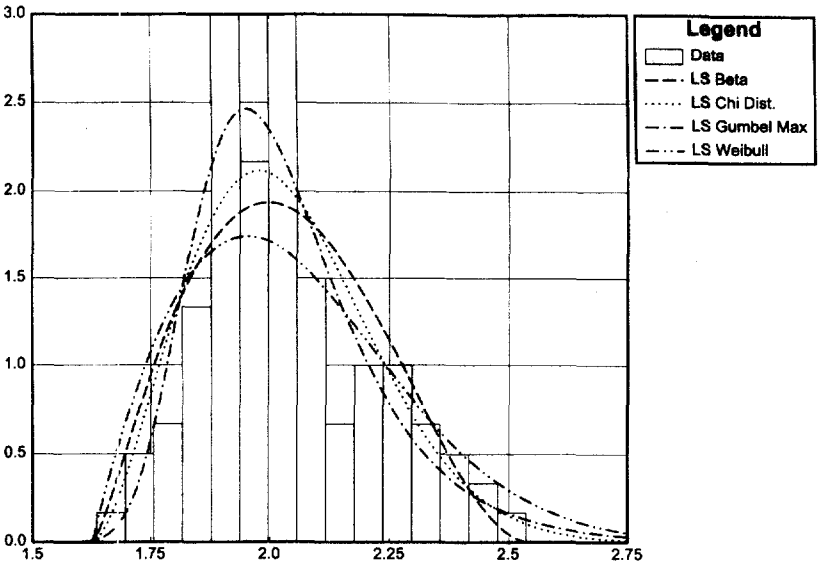

b)

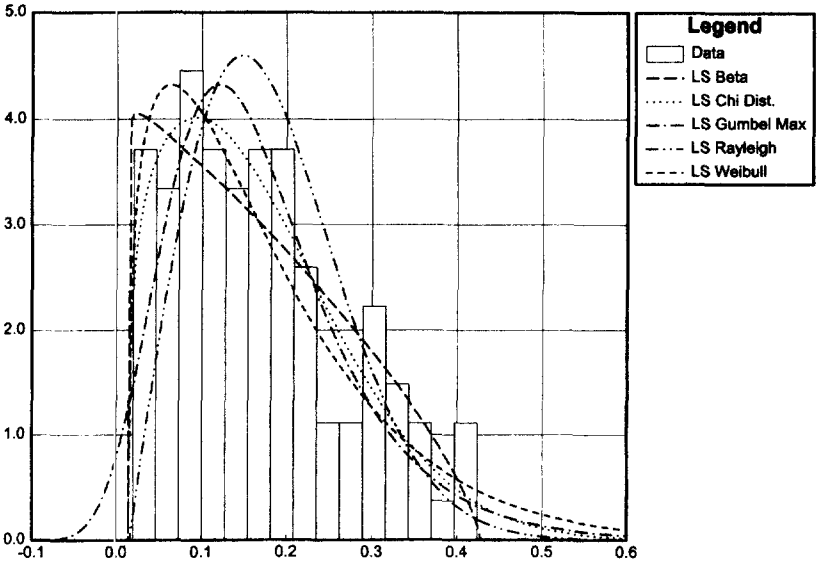

Fig. 6. Probability densities of $C_{ii}/2$ (a) and $C_{12,\max}$ (b) of the disk–matrix composite of Fig. 1 at contrast 100.

$$f_m : \mathbf{R}^2 \times \Omega \to \{0, 1\}. \tag{31}$$

That is, the random composite material **B** is described by a set $\{f_m(\omega)\,;\,\omega \in \Omega\}$ of realizations $f_m(\omega)$. On the technical side, $f_m(\mathbf{x}, \omega)$ is a discrete random field with a continuous parameter because it is discrete in Ω and continuous in $\mathbf{R}^2$. Material properties are given in terms of a random field

$$\mathbf{C} : \mathbf{R}^2 \times \Omega \to \{C^{(m)}\mathbf{I}, C^{(f)}\mathbf{I}\}. \tag{32}$$

Clearly, the random field $\{\mathbf{C}(\mathbf{x}, \omega)\,;\ x \in B, \omega \in \Omega\}$ is also discrete with a continuous parameter, as illustrated in Fig. 8 in terms of one realization along the x_1-axis.

In view of the considerations leading to the derivation of the δ-dependent hierarchy of bounds (11), at any point **x** in the material and at any meso-scale δ, two estimates of

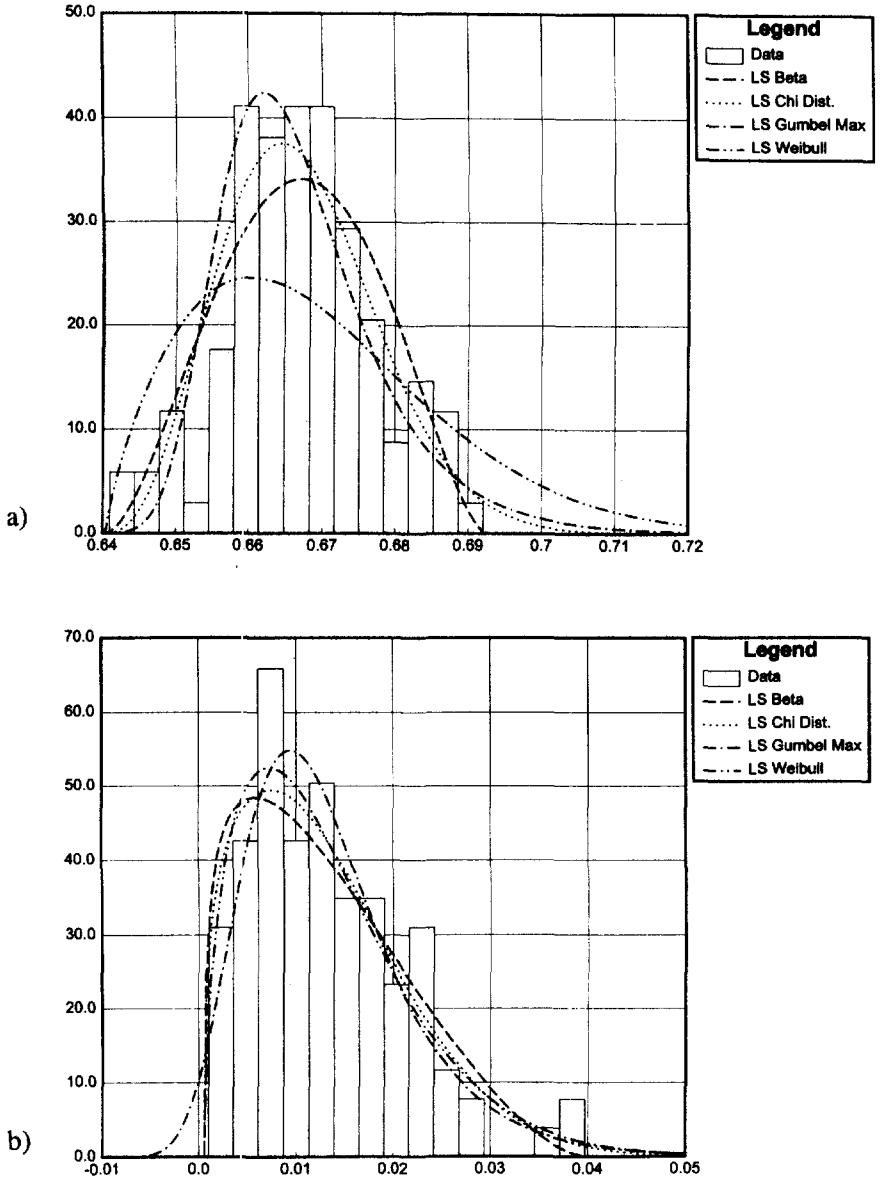

Fig. 7. Probability densities of $S_{ii}/2$ (a) and $S_{12,\max}$ (b) of the disk–matrix composite of Fig. 1 at contrast 100.

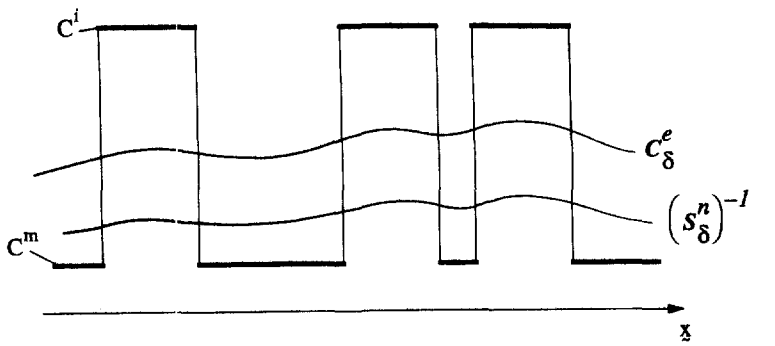

Fig. 8. The setup of random fields: from a piecewise-constant realization of a composite to two approximating continua at a non-zero, finite mesoscale δ.

effective properties may be introduced: $\mathbf{C}_\delta^e$ and $\mathbf{C}_\delta^n \equiv (\mathbf{S}_\delta^n)^{-1}$. Consequently, at any meso-scale δ there are two approximating tensor-valued random fields

$$\mathbf{C}_\delta^e : \mathbf{R}^2 \times \Omega \to \mathbf{R}^3 \quad \mathbf{S}_\delta^n : \mathbf{R}^2 \times \Omega \to \mathbf{R}^3. \tag{33}$$

We readily observe that these two *meso-scale random fields* are continuous with a continuous parameter because each mapping in eqn (33) is continuous in the set $\mathbf{R}^2 \times \Omega$. Any specific composite material **B** is now described, in an approximate way, by two sets of realizations: $\{\mathbf{C}_\delta^e(\mathbf{x}, \omega)\}$ and $\{\mathbf{S}_\delta^n(\mathbf{x}, \omega)\}$ (see Fig. 8). This approximation, which depends directly on the choice of δ, provides two alternate inputs to a field equation governing the global response

$$[\mathbf{C}_{ij}(\mathbf{x}, \omega) u_j]_{,i} = 0. \tag{34}$$

One way to determine the global response is described below.

4.3. *Comments on the stochastic finite element method*

It has been shown in (Ostoja-Starzewski, 1993b; Alzebdeh and Ostoja-Starzewski, 1993, 1996) that the foregoing setup of two random fields allows a micromechanically based formulation of *stochastic finite elements* (SFE). In essence, the meso-scale window corresponds to a single finite element and thus, depending on the boundary conditions employed for its Hooke's law determination, either a stiffness matrix is found from (7) or a flexibility matrix is found from (8). Thus, the random fields (33) provide two bounds on the global response of a random medium, the larger the meso-scale, the narrower are the bounds, albeit the possibility of resolution of local detail is being lost.

If the solutions of the Dirichlet and Neumann boundary value problems were replaced by the uniform strain and uniform stress assumptions, the meso-scale properties would be given in terms of the Voigt and Reuss-type volume averages over given meso-scale windows. This would then reduce the above formulation to a so-called *local averaging of random fields* (Vanmarcke, 1983). Local averaging over a single finite element domain has often been employed in setting up of random stiffness matrices in the SFE. It is clear from our micromechanics considerations that in such an approach two very different outputs are obtained because the Voigt and Reuss bounds are very crude.

Indeed, many present SFE studies either employ just one of these local averages as the input to an SFE program, or use some other intuitive averaging scheme, or postulate a so-called weighted residual method as an improved estimate of the stiffness matrix at the finite element level [e.g. Deodatis and Graham (1996)]. A comprehensive review of the SFE literature up to the early nineties has been provided in Brenner (1991), several books have been written (Ghanem and Spanos, 1991; Kleiber and Hien, 1993), and the most recent status of research is given in a number of conference papers in (Frangopol and Girgoriu, 1996). Clearly, without a micromechanical analysis such approaches cannot be right because the knowledge of scale dependence, and two random fields, not just one, are needed to bound the global response. Furthermore, these SFE studies always begin with a random medium defined by a continuous random field of two elastic moduli such as Young's modulus E and Poisson's ratio ν. Existence of such a material is the subject of the next section.

4.4. *On the existence of locally isotropic, inhomogeneous, smooth elastic materials*

There is no question that one can set up a mathematical model of a locally isotropic, inhomogeneous, smooth elastic material. However, the physical existence of a microstructure that would guarantee a spatial gradient together with a locally isotropic behavior appears questionable. To this end, let us consider the simplest case of a gradient of material properties in one direction only, say x_1. If we have two locally isotropic phases at our

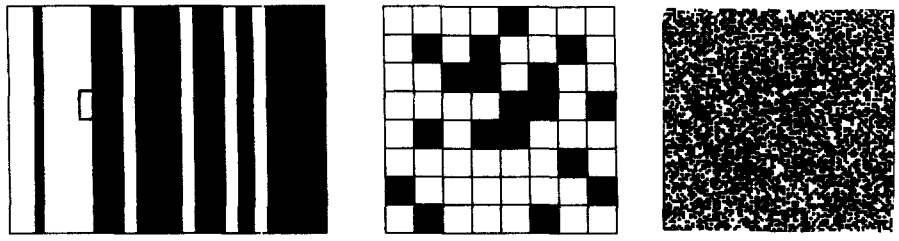

a) b) c)

Fig. 9. A finite size window in a layered microstructure (a); a two-phase disordered chessboard of size 8×8 (b) and 100×100 (c).

disposal ($C^{(1)}$, $C^{(2)}$), this can be realized by considering a layered medium, Fig. 9(a); width of a single layer is the microscale d in the problem. Clearly, the material is piecewise constant, and a meso-scale window offers a way to introduce a smooth approximation. We must have $\delta > 0$, or else jumps would reappear. If the window falls entirely in either one of the phases, the local property $\mathbf{C}_\delta$ is locally isotropic, either $C^{(1)}\mathbf{I}$ or $C^{(2)}\mathbf{I}$. If the window straddles a boundary between the phases, the property $\mathbf{C}_\delta$ is locally orthotropic with diagonal components given exactly by the Voigt and Reuss estimates for the C_{22} and the C_{11}, respectively.

Let us next consider the case of a random chessboard with spatially homogeneous and isotropic statistics, and both phases locally isotropic, Fig. 9(b). Again, the local property $\mathbf{C}_\delta$ can be determined by introducing a meso-scale window. We see now that on scales $\delta > 0$ a similar analysis as for a layered material above applies. On scales $\delta > 1$ neither a Voigt nor a Reuss estimate is correct, but, rather, a solution in the vein of Section 2 needs to be carried out, leading to $\mathbf{C}_\delta^e$ and $\mathbf{C}_\delta'' \equiv (\mathbf{S}_\delta'')$ both of which are "usually" anisotropic. Suppose we have a window which yields a locally isotropic behavior. As we move it in a certain direction, we immediately change the microstructure in an anisotropic manner because of the spatial disorder of any given realization $\mathbf{B}(\omega)$, and so the isotropy is lost. Additionally, two estimates of the local response are available, a fact which contradicts the postulate of a unique continuum model. As δ increases to infinity, these two estimates begin to converge to one another in the homogenization limit described by (11), but then the spatial gradient vanishes.

Turning to the matrix–inclusion composite, we note than on scales $\delta > 1$ a locally isotropic response would only be obtained for perfectly periodic disk arrangements with respect to the mesoscale windows, but this can occur only with a probability of zero, since it involves sets in $\mathbf{R}^2$ of Lebesgue measure zero. We thus have three possible cases:

- if the statistics of the microstructure are homogeneous and isotropic, an isotropic material is obtained in the $\delta \to \infty$ limit, while on finite scales two random fields are available, whose realizations are isotropic with probability zero;
- if the statistics of the microstructure are homogeneous and anisotropic, an anisotropic material is obtained in the $\delta \to \infty$ limit, while on finite scales two random fields are available, whose realizations can be isotropic with probability zero;
- if the statistics of the microstructure are inhomogeneous, an anisotropic (typically orthotropic) material is obtained in the large δ limit; the $\delta \to \infty$ limit has to be approached carefully as the length scale of global inhomogeneity is, in principle, finite. On finite scales two random fields are available, whose realizations can be isotropic only with probability zero [e.g. Ostoja-Starzewski *et al.* (1994)].

It is noteworthy, however, that special cases of locally isotropic, inhomogeneous, smooth elastic materials can be constructed; for example, a thermoelastic material in an inhomogeneous temperature field would exhibit smooth variability of its properties.

4.5. *On the correlation structure of meso-scale random fields*

Application of micromechanics in stochastic finite elements requires, besides the specification of one-point statistics of meso-scale moduli, a specification of their spatial correlations, so as to allow a rapid assignment of properties to all the elements given their relative spatial locations. That is, if we consider the random field $\mathbf{C}$, which stands either for $\mathbf{C}^{\mathrm{e}}_{\delta}$ and $\mathbf{S}^{n}_{\delta}$, we should have some prescriptions for the autocorrelations of its three components as well as their three cross-correlations. Its spatial structure is described, to second-order, by a *correlation coefficient*

$$\rho_{\mathbf{C}_{ij}\mathbf{C}_{kl}}(\mathbf{x},\mathbf{x}') = \frac{\langle \mathbf{C}_{ij}(\mathbf{x})\mathbf{C}_{kl}(\mathbf{x}')\rangle - \langle \mathbf{C}_{ij}(\mathbf{x})\rangle\langle \mathbf{C}_{kl}(\mathbf{x}')\rangle}{\sigma_{\mathbf{C}_{ij}}(\mathbf{x})\sigma_{\mathbf{C}_{kl}}(\mathbf{x}')} \tag{35}$$

where all $\mathbf{C}_{ij}$ and $\mathbf{C}_{kl}$ stand for either $\mathbf{C}^{\mathrm{e}}_{ij}$ and $\mathbf{C}^{\mathrm{e}}_{kl}$ or $\mathbf{S}^{\mathrm{n}}_{ij}$ and $\mathbf{S}^{\mathrm{n}}_{kl}$, while σs are standard deviations. For a composite having stationary statistics of its properties, such as its indicator function (24), the random field $\mathbf{C}(\mathbf{x})$ is wide sense stationary, i.e.

$$\rho_{\mathbf{C}_{ij}\mathbf{C}_{kl}}(\mathbf{x},\mathbf{x}') = \rho_{\mathbf{C}_{ij}\mathbf{C}_{kl}}(\mathbf{r}) \quad \mathbf{r} = \mathbf{x}-\mathbf{x}'. \tag{36}$$

A natural question arises here: is the $\mathbf{C}$ field isotropic in terms of its correlation function? (This is, of course, different from the isotropy of its realizations.) Our computations, based on cross-correlating a window placed at $\mathbf{x}$ with a window fixed at the origin of the coordinate system, indicate that $\mathbf{C}$ is a *quasi-isotropic* random field. In terms of a specific component of $\mathbf{C}$, say C_{ij}, this means that the equality $|\mathbf{r}| = \|\mathbf{s}\|$ implies

$$\rho_{\mathbf{C}_{ij}\mathbf{C}_{kl}}(\mathbf{r}) = \rho_{\mathbf{C}_{ij}\mathbf{C}_{kl}}(\mathbf{s}) \tag{37}$$

where ρ is the autocorrelation function of C_{ij} and $\mathbf{s}$ is given by an invertible transformation

$$\mathbf{s} = T(\mathbf{r}) = [T_1(\mathbf{r}), T_2(\mathbf{r})] \quad \mathbf{r} = (r_1, r_2) \tag{38}$$

of $\mathbf{R}^2$ into $\mathbf{R}^2$. Here by $|\mathbf{r}|$ we denote a norm in $\mathbf{R}^2$ and by $\|\mathbf{s}\|$ a norm in $\mathbf{R}^2$ after the transformation.

A particularly good approximation is obtained in the special case of such a quasi-isotropic field: an elliptic correlation function which is specified by a quadratic form $[b_{mn}]$ having the positive definiteness property

$$\|s\| = \sum_{i,j=1}^{2} s_i b_{ij} s_j > 0. \tag{39}$$

This means that the transformation (38) takes the surface of a circle $\Sigma^2_{i,j=1} r_i r_j = R^2$ into that of an ellipse $\Sigma^2_{i,j=1} s_i b_{ij} s_j = P^2$. Next, it turns out that, for composite systems modeled by point processes of Poisson type, the range of these correlations is limited to the window size L plus a couple of inclusion's diameters; the latter contribution is due to the disks which straddle the boundary between two contiguous windows/elements, whereas in the case of needles, their lengths play the role of the diameter. Clearly, the inherent independence property of the Poisson point placement process precludes the correlations from being long range such as typically assumed through exponential correlation functions in the SFE literature. The above model may be applied to auto- and cross-correlations between all the components of $\mathbf{C}$; specific details for pixel systems and disk–matrix composites were given in (Ostoja–Starzewski, 1994).

In the above we treated each of the components of the $\mathbf{C}$-field separately. It is possible, however, to consider a different interpretation of stationarity and isotropy. Namely, following Yaglom (1957), we ask whether the second-order tensor field $\mathbf{C}$, i.e. either $\mathbf{C}^{\mathrm{e}}_{\delta}$ or $\mathbf{S}^{n}_{\delta}$, is stationary and isotropic in the sense that $\rho_{\mathbf{C}_{ij}\mathbf{C}_{kl}}(\mathbf{r})$ does not change upon the rotation

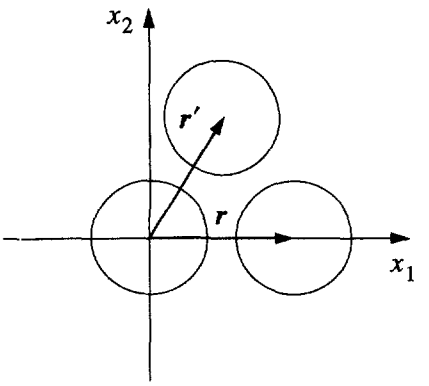

Fig. 10. Three meso-scale windows illustrating the concept of stationarity and isotropy in the sense of eqn (40).

of $\mathbf{r}$ into $\mathbf{r}'$, which is accompanied by an appropriate transformation of $\mathbf{C}$ into $\mathbf{C}'$ corresponding to this rotation. In other words, field $\mathbf{C}$ is now called *stationary and isotropic* if

$$\langle \mathbf{C}' \rangle = QQ\langle \mathbf{C} \rangle \quad \rho(\mathbf{r}') = QQ\rho(\mathbf{r}) \tag{40}$$

where Q is a well-known linear transformation giving $\mathbf{C}'$

$$\mathbf{C}' = QQ\mathbf{C}. \tag{41}$$

Now, with reference to Fig. 10, we consider a mesoscale window fixed, without loss of generality, at the origin of the Ox_1x_2-system, and two other windows placed at $\mathbf{r}$ and $\mathbf{r}'$, respectively. By taking circular-shaped meso-scale windows we ensure that eqn (40) is satisfied, provided that the random field of material properties [eqn (32)] is stationary and isotropic. It is interesting to note that the computational method for determining effective moduli of composite materials with circular inclusions due to Bird and Steele (1992) is suited for analysis of this type of stationarity and isotropy.

5. RANDOM CHESSBOARDS AND BERNOULLI LATTICES

A simplest approximation of random chessboards, shown in Fig. 9(b), is available by considering just one degree-of-freedom per single board. In this case we are dealing with a *Bernoulli lattice process* $\Phi_{p,a}$ on a Cartesian lattice of spacing a with each point of this lattice being of type 1 (or 2) with probability $p(q = 1-p)$ independently of all the other points (Stoyan *et al.*, 1987). If the random variable $\Phi_{p,a}(B)$ is the number of points in B then it is binomially distributed with parameters p and n (the number of lattice points that belong to B). Also, $\Phi_{p,a}(B_1)$, $\Phi_{p,a}(B_2), \ldots, \Phi_{p,a}(B_k)$ are independent if $B_1, B_2, \ldots, B_k$ are pairwise disjoint, and we have

$$P(\Phi_{p,a}(B) = k) = \binom{n}{k} p^k q^{(n-k)}. \tag{42}$$

Evidently, p and q define the volume fractions of both types of phases (1 and 2).

Since, graphically, this represents one pixel per one board, we may also call it a *binary pixel system*, Fig. 9(c). Clearly, the local stress and strain concentrations cannot be resolved, but the statistics of such simple systems give an indication of the statistics of random chessboards. Conductivity of such a system is, perhaps, the simplest setup in which to investigate the scale dependence of the ensemble average estimates based on the essential

and natural boundary conditions. The latter problem is somewhat akin to a so-called *finite-size scaling* in statistical physics (Cardy, 1988), but the attention in that area has always been focused on the phase transition problems.

In Ostoja-Starzewski and Schulte (1996) we studied the finite-size scaling of $\langle \mathbf{C}_\delta^e \rangle$ and $\langle \mathbf{S}_\delta^n \rangle^{-1}$ for Bernoulli lattices at 50% volume fraction of either phase, and found it to be of the form

$$\langle \mathbf{C}_\delta^e \rangle \sim \exp(-\delta^{-p}) \quad \langle \mathbf{S}_\delta^n \rangle^{-1} \sim \exp(\delta^{-q}) \tag{43}$$

where p and q are functions of the contrast α

$$p(\alpha) = 3.8\alpha^{0.14} \quad q(\alpha) = 2.4\alpha^{0.59}. \tag{44}$$

These results are obtained from computations over a range of scales 1–1000. While the smallest scale can be calculated explicitly as the Voigt and Reuss bounds, the largest involved a lattice of 1000×1000 nodes, i.e. having one million degrees-of-freedom. The parameter space of contrast and volume fraction is vast and, therefore, only select cases can be run numerically at these large scales. Based on such select runs, we can presently conjecture that the scaling laws (43) apply for other volume fractions than 50%, with (44) being replaced by

$$p(\alpha) \approx \alpha^{r_1} \quad q(\alpha) \approx \alpha^{r_2} \tag{45}$$

where r_1 and r_2 depend on the volume fraction.

The Bernoulli lattice at a volume fraction below $\sim 30\%$ can also be interpreted as a very crude model of a disk–matrix composite, again with one degree-of-freedom per disk. Given the fact that a more realistic spring network model requires several (at least five) lattice spacings per disk, a lattice of some 5000×5000 nodes (25 million degrees-of-freedom) would have to be run. Thus, the above scaling laws provide the best available indication of finite-size scaling of both bounds, $\langle \mathbf{C}_\delta^e \rangle$ and $\langle \mathbf{S}_\delta^n \rangle^{-1}$, of disk–matrix composites.

The foregoing statement can be supported by a comparison of the statistics of random tensors $\mathbf{C}_\delta^e$ and $\mathbf{S}_\delta^n$ of the disk–matrix systems (Figs 6 and 7) on one hand, with those of the binary pixel systems on the other. Thus, Fig. 11(a, b) show half the trace $C_{ii}/2$ and the Mohr's circle radius $C_{12,\max}$. Next, Fig. 12(a, b) show half the trace $S_{ii}/2$ and the Mohr's circle radius $S_{12,\max}$. These plots correspond to a scale $\delta = 100$, volume fractions of either phase 50%, and contrast 10^4. We first note the positive skewness of both traces, with the skewness of the trace resulting from essential boundary conditions being stronger than that of the natural ones. Furthermore, the maximum shear components are qualitatively very similar to those shown in Figs 6(b) and 7(b). In all the cases we show the best possible fits obtainable from several basic probability distributions, such as beta, χ^2, Rayleigh, Gumbel and Weibull.

6. ELLIPSE/NEEDLE SYSTEMS

6.1. *Generation via a random fiber process*

In order to generate a field of ellipses or needles, we proceed in the following steps.

Step 1: Generate Poisson points in $\mathbf{R}^2$ in the same way as described in Section 3.1.

Step 2: Generate an angle θ from $[0, \pi]$ according to a probability density

$$f(\theta) = \frac{1}{\pi}(1 + a_1 \cos 2\theta + a_2 \cos 4\theta + , \ldots , + a_n \cos 2n\theta) \tag{46}$$

where θ is the line of inclination of the line to the x-axis. In simulations we usually take only the first term in the cosine series (46); in practice, where fitting of experimental data

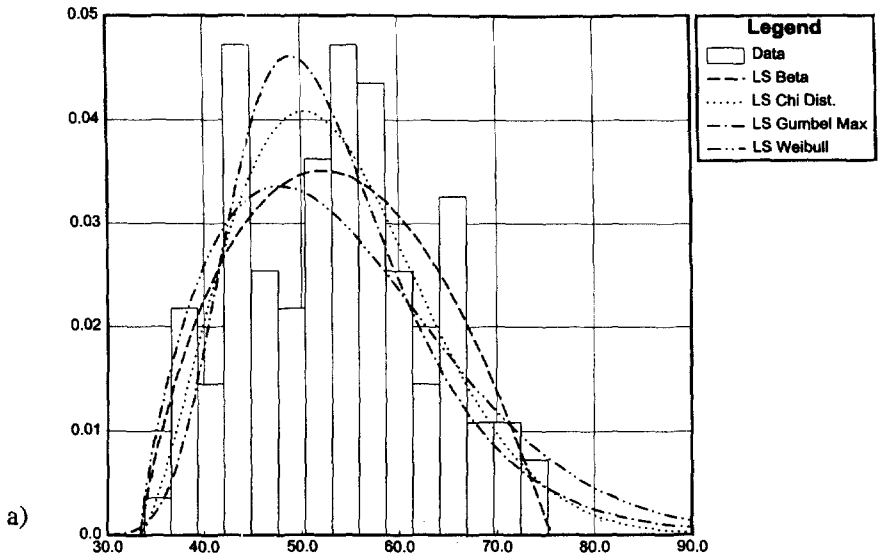

a)

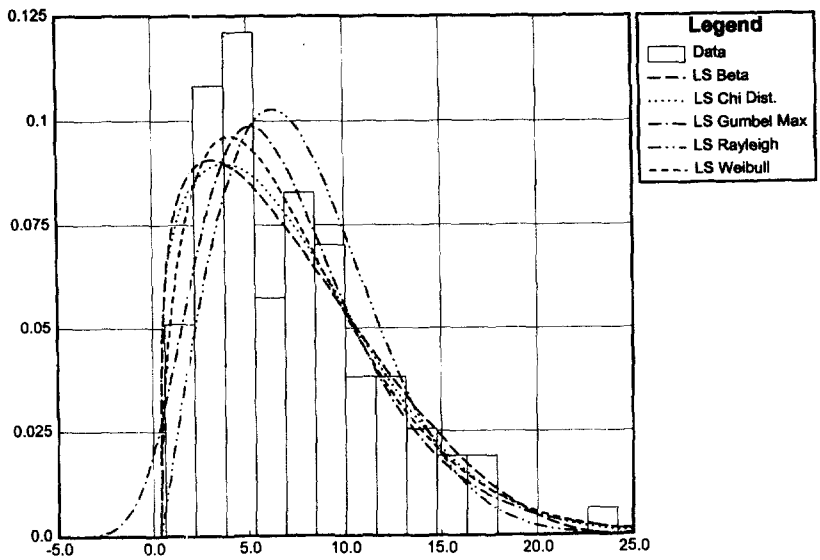

b)

Fig. 11. Probability densities of $C_{ii}/2$ (a) and $C_{12,\max}$ (b) of Bernoulli lattice such as that shown in Fig. 9(c) at: scale $\delta = 100$, volume fraction of either phase 50%, and contrast 10^4.

is needed, either more terms need to be included, or other types of distributions can be considered [e.g. Mark (1984)].

Step 3: A line of length l according to a probability density $p(l)$ is generated, which results in two vectors $\mathbf{n}$ and $\mathbf{m}$ along the major and minor semi-axes of the ellipse, respectively [Fig. 13(a)]. Note that the subset of $\mathbf{R}^2$ on which the binomial process is conducted must be larger than the actual window domain which will be tested for effective moduli, lines that originated from Poisson points outside the window, located up to a distance $l/2$, should be accounted for.

A realization of an isotropic field of 1000 needles of a length of 10 units and a thickness of 1 unit in a 1000×1000 window is shown in Fig. 14. Already at this low density, random clustering of needles is easily seen, it gives rise to relatively stronger fluctuations of meso-scale moduli than in the case of round disks having the same cumulative volume fraction. As the aspect ratio increases, these fluctuations grow.

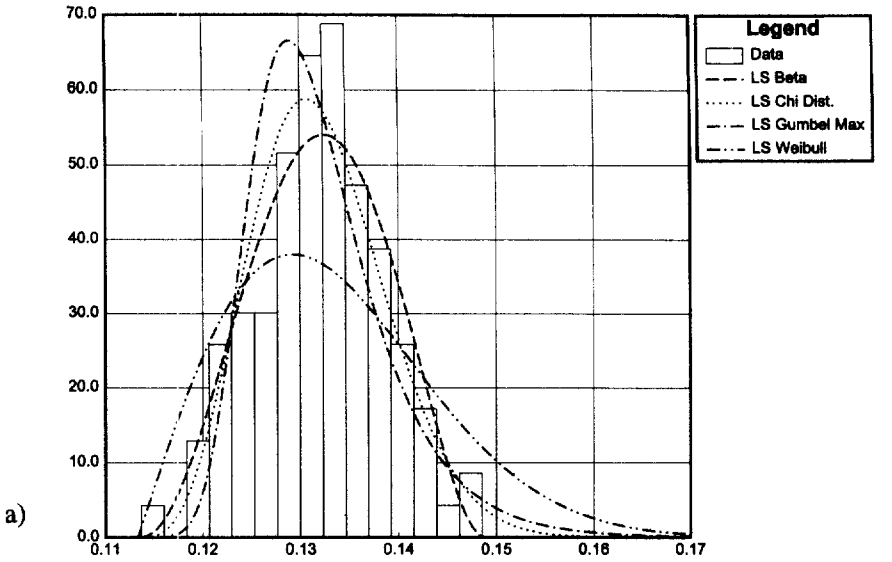

a)

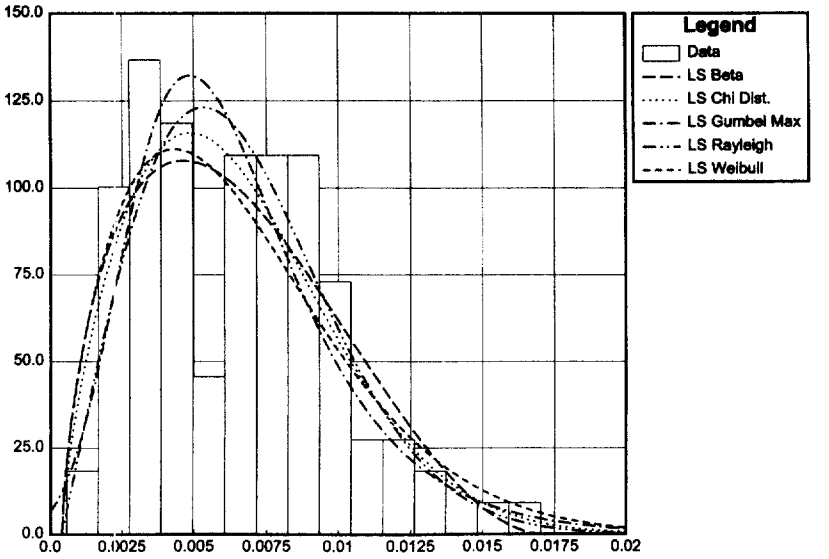

b)

Fig. 12. Probability densities of $S_{ii}/2$ (a) and $S_{12,\max}$ (b) of a Bernoulli lattice such as that shown in Fig. 9(c) at scale $\delta = 100$, volume fraction of either phase 50%, and contrast 10^4.

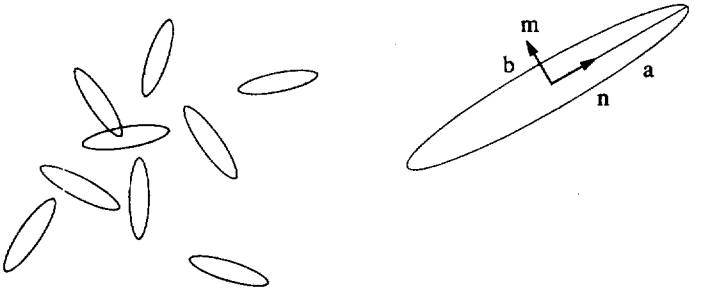

a) b)

Fig. 13. (a) Randomly located ellipses, with overlap permitted: (b) basis for a fabric tensor.

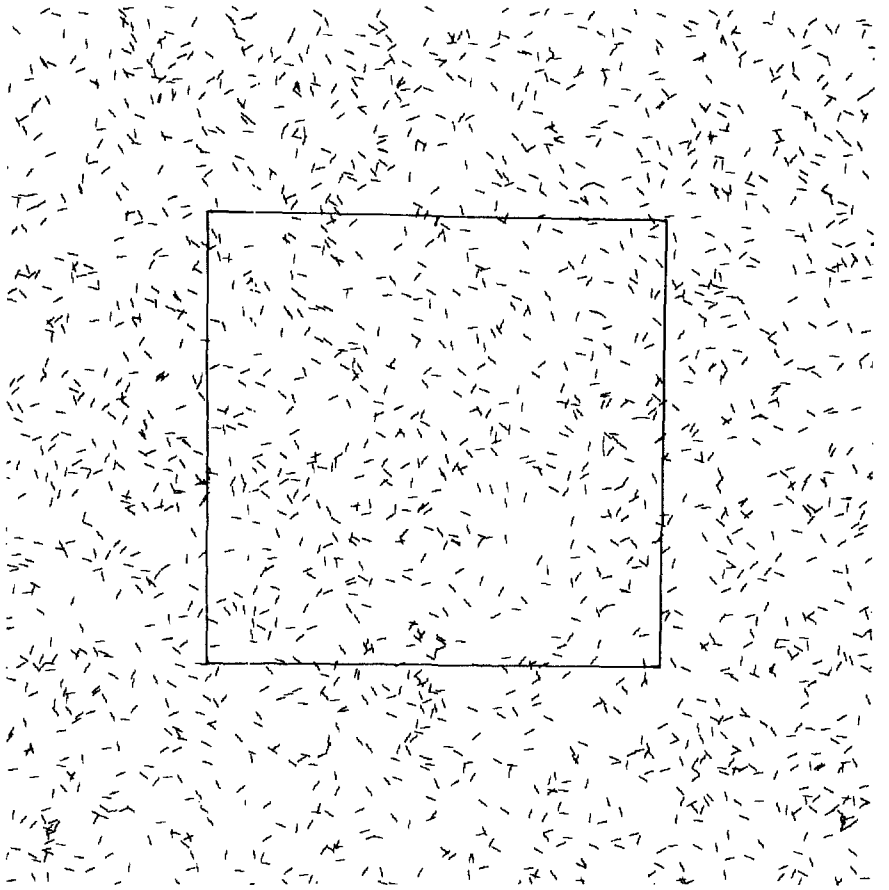

Fig. 14. A 1000×1000 window of 1000 randomly located 10×1 needles with an isotropic distribution. A subwindow of size 500×500 (scale $\delta = 50$) is indicated.

6.2. *Cross-correlations of the meso-scale moduli with the crack density tensor*

Studies on effective moduli of materials with cracks of ellipsoidal, or elliptical, pores rely on a crack density tensor (Kachanov, 1972), which may be called a *fabric tensor*:

$$\beta_{ij} = \frac{\pi}{A}\sum_k (a^2 n_i n_j + b^2 m_i m_j)^{(k)}. \tag{47}$$

Work on effective moduli of materials with microcracks dates back to Budiansky and O'Connell (1976), while a recent review was given by Kachanov (1993); some of the earliest ideas were presented in (Vakulenko and Kachanov, 1971). Recently, an experimental confirmation of the results of an effective medium (Mori–Tanaka) theory for low crack densities, typically employed by Kachanov, has been given in Carvalho and Labuz (1996).

The effective medium theory, however, cannot say anything about the finite size scaling of effective moduli and their statistics; nor is it reliable for higher crack densities. On the other hand, these problems can be treated by the method already outlined for other materials in previous sections, and so, we give in Fig. 15(a, b) the scaling of moduli $\langle \mathbf{C}_\delta^e \rangle$ and $\langle \mathbf{S}_\delta^n \rangle^{-1}$ for needle systems of contrasts 10^{-2} and 10^{-4}. It is interesting to note here the same type of slow approach, especially that of the upper bound, to an RVE as observed earlier for soft disk systems (Fig. 4).

In the following, we shall also investigate the correlation structure of the system at hand. To this end, we will look at the β_{ij} tensor *vis-à-vis* the meso-scale response tensors

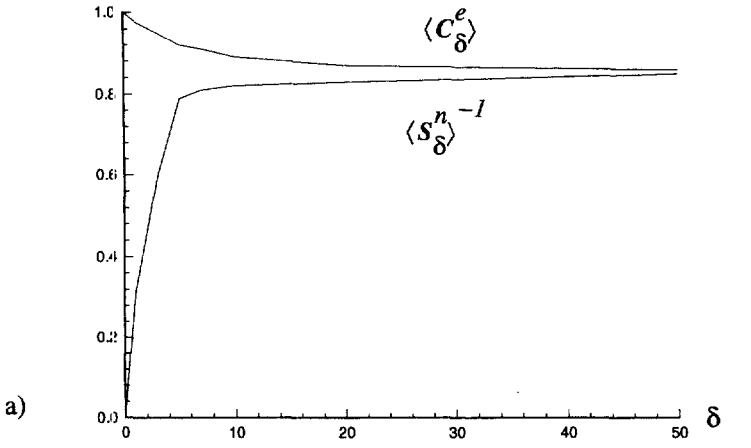

Fig. 15. A hierarchy of scale dependent bounds, normalized by $C^{(m)} = 1$, of stiffnesses of the needle–matrix composite of Fig. 14 at contrasts 10^{-2} (a), and 10^{-4} (b).

C^e_{kl} and S^n_{kl}, where, for simplification of notation we suppress the δ parameter. This will be done via a cross-correlation function

$$R_{\beta_{ij}C_{kl}} = \langle \beta_{ij} C_{kl} \rangle - \langle \beta_{ij} \rangle \langle C_{kl} \rangle \tag{48}$$

where C_{kl} stands for either C^e_{kl} or S^n_{kl}. It will be even more convenient to use a correlation coefficient

$$\rho_{\beta_{ij}C_{kl}} = \frac{\langle \beta_{ij} C_{kl} \rangle - \langle \beta_{ij} \rangle \langle C_{kl} \rangle}{\sigma_{\beta_{ij}} \sigma_{C_{kl}}} \tag{49}$$

which normalizes $R_{\beta_{ij}C_{kl}}$ by the standard deviations of C^e_{kl} and S^n_{kl}.

Our computations, given the vast extent of the parameter space, have, so far, been restricted. However, some interesting trends could be observed. For example, isotropic systems [$a_1 = 0$ in (46)] of soft needles (contrast 0.1) of aspect ratios 10 and 20 at window sizes $\delta = 5$ and 10, show that the following fabric-property cross-correlations hold

$$\rho_{\boldsymbol{\beta}_{ij}\mathbf{C}^{\mathrm{e}}_{ij}} \equiv \begin{bmatrix} \rho_{\beta_{11}C^{\mathrm{e}}_{11}} > 0, & \rho_{\beta_{12}C^{\mathrm{e}}_{11}} < 0, & \rho_{\beta_{22}C^{\mathrm{e}}_{11}} > 0 \\ \rho_{\beta_{11}C^{\mathrm{e}}_{12}} > 0, & \rho_{\beta_{12}C^{\mathrm{e}}_{12}} < 0, & \rho_{\beta_{22}C^{\mathrm{e}}_{12}} > 0 \\ \rho_{\beta_{11}C^{\mathrm{e}}_{22}} > 0, & \rho_{\beta_{12}C^{\mathrm{e}}_{22}} < 0, & \rho_{\beta_{22}C^{\mathrm{e}}_{22}} > 0 \end{bmatrix}$$

$$\rho_{\boldsymbol{\beta}_{ij}\mathbf{S}^{\mathrm{n}}_{ij}} \equiv \begin{bmatrix} \rho_{\beta_{11}S^{\mathrm{n}}_{11}} < 0, & \rho_{\beta_{12}S^{\mathrm{n}}_{11}} > 0, & \rho_{\beta_{22}S^{\mathrm{n}}_{11}} < 0 \\ \rho_{\beta_{11}S^{\mathrm{n}}_{12}} < 0, & \rho_{\beta_{12}S^{\mathrm{n}}_{12}} > 0, & \rho_{\beta_{22}S^{\mathrm{n}}_{12}} < 0 \\ \rho_{\beta_{11}S^{\mathrm{n}}_{22}} < 0, & \rho_{\beta_{12}S^{\mathrm{n}}_{22}} > 0, & \rho_{\beta_{22}S^{\mathrm{n}}_{2}} < 0 \end{bmatrix}. \tag{50}$$

On the other hand, the introduction of anisotropy ($a_1 = 1$) in such systems with all the other parameters held fixed leads to these fabric-property cross-correlations.

$$\rho_{\beta_{ij}\mathbf{C}^{\mathrm{e}}_{ij}} \equiv \begin{bmatrix} \rho_{\beta_{11}C^{\mathrm{e}}_{11}} < 0, & \rho_{\beta_{12}C^{\mathrm{e}}_{11}} > 0, & \rho_{\beta_{22}C^{\mathrm{e}}_{11}} < 0 \\ \rho_{\beta_{11}C^{\mathrm{e}}_{12}} < 0, & \rho_{\beta_{12}C^{\mathrm{e}}_{12}} > 0, & \rho_{\beta_{22}C^{\mathrm{e}}_{12}} < 0 \\ \rho_{\beta_{11}C^{\mathrm{e}}_{22}} > 0, & \rho_{\beta_{12}C^{\mathrm{e}}_{22}} < 0, & \rho_{\beta_{22}C^{\mathrm{e}}_{22}} > 0 \end{bmatrix}$$

$$\rho_{\boldsymbol{\beta}_{ij}\mathbf{S}^{\mathrm{n}}_{ij}} \equiv \begin{bmatrix} \rho_{\beta_{11}S^{\mathrm{n}}_{11}} > 0, & \rho_{\beta_{12}S^{\mathrm{n}}_{11}} < 0, & \rho_{\beta_{22}S^{\mathrm{n}}_{11}} > 0 \\ \rho_{\beta_{11}S^{\mathrm{n}}_{12}} > 0, & \rho_{\beta_{12}S^{\mathrm{n}}_{12}} < 0, & \rho_{\beta_{22}S^{\mathrm{n}}_{12}} > 0 \\ \rho_{\beta_{11}S^{\mathrm{n}}_{22}} < 0, & \rho_{\beta_{12}S^{\mathrm{n}}_{22}} > 0, & \rho_{\beta_{22}S^{\mathrm{n}}_{22}} < 0 \end{bmatrix}. \tag{51}$$

This implies that for finite windows the correlation of β_{ij} with C^{e}_{kl} tends to be opposite in sign to that of $\boldsymbol{\beta}_{ij}$ with S^{n}_{kl}.

$$\rho_{\beta_{ij}C^{\mathrm{e}}_{ij}} = -\rho_{\beta_{ij}S^{\mathrm{e}}_{ij}} \tag{52}$$

Now, C^{e}_{kl} and S^{n}_{kl} must converge to the macroscopic, deterministic $C^{\mathrm{eff}}_{kl}|_{\delta\to\infty}$, so that the only way that (52) may hold is for β_{ij} to become uncorrelated with $\mathbf{C}^{\mathrm{e}}_{\delta}$ and $\mathbf{S}^{n}_{\delta}$ in the large scale limit $\delta \to \infty$. This implies that the second-order moments of geometry of a material with cracks, such as the conventional fabric tensor β_{ij}, may be insufficient in describing macroscopic structure–property relations. In other words, one has to look at higher moments and other geometric measures of the crack network connectivity.

7. FIBER SYSTEMS

We complete the present discussion of the parameter map of Fig. 2(c) with selected results on in-plane conductivities of cellulose fiber networks. Such networks are presently being employed to model paper, the topic is vast by itself, but the goal of this section is to show that a lot of issues may be approached from the same perspective as adopted at the outset of this paper. Thus, although paper comprises some seven to ten fiber thicknesses, it will be sufficient to focus here on a quasi-single-layer fiber structure. The simple mechanism for generation of random fiber networks is based on a planar Poisson point process with inhibition of Section 6.1. The point is that by varying $d_{\min}$ we can change the degree of fiber clustering (so-called *flocculation*) in the network, a very important consideration in paper manufacturing processes. Thus, in Fig. 16(a) we show a network generated without any restriction on the distance of Poisson points: $d_{\min} = 0$; fiber angles were sampled from the distribution (46) with $a_1 = 1$; fiber lengths were sampled from a uniform distribution according to a rule: $l = \langle l \rangle (1+r)$, with a random number $r \in [-0.5, 0.5]$ and $\langle l \rangle = 1.2$ mm; fiber widths being 0.03 mm. By contrast, the network of Fig. 15(b) is less disordered due to the assumption $d_{\min} = \langle l \rangle / 20 = 0.24$ mm.

The hierarchy of bounds (11) is now developed for the network of Fig. 16(b) with $C^{\mathrm{fiber}} = 5C^{\mathrm{void}}$; in Fig. 17(a). However, these two Cs are interpreted here as thermal conductivities of the fiber and void phases, respectively; both are assumed to be locally isotropic. Note that there is an anisotropy in the material due to the assumption of the

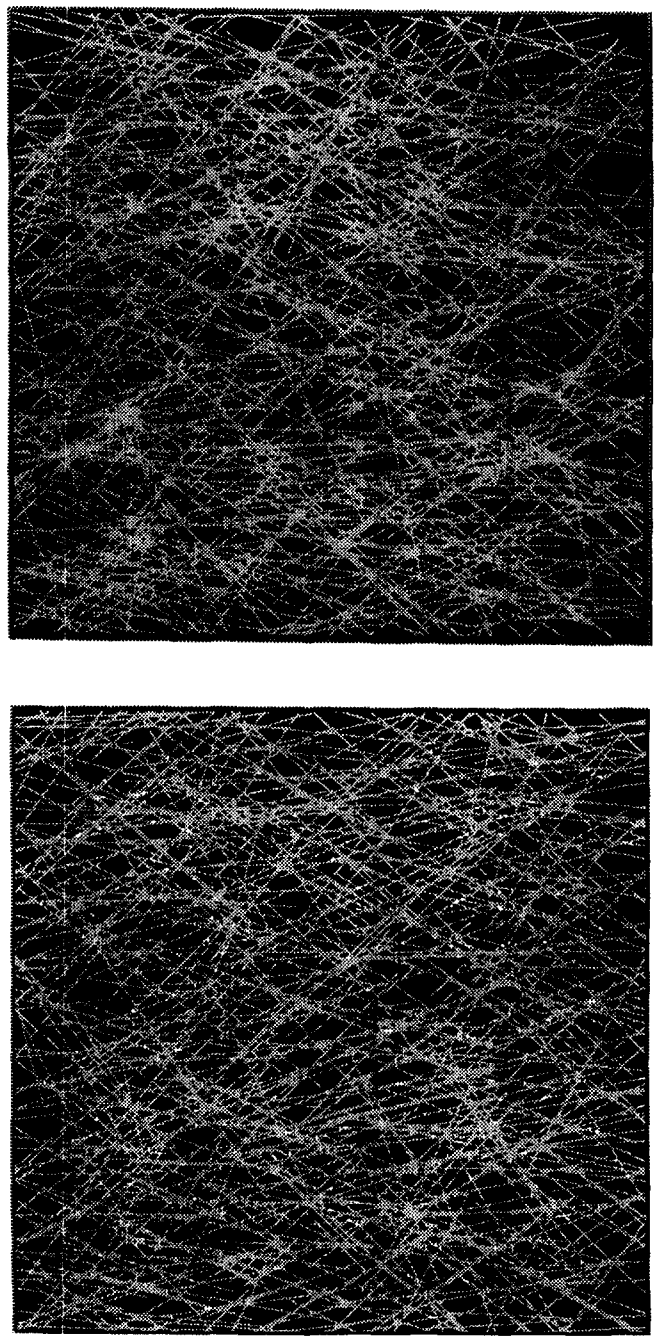

Fig. 16. (a) A realization of a random, anisotropic fiber network, with small disks of radius $d_{\min} = 0.24$ mm, signifying the mutual inclusion of Poisson points; $\langle l \rangle = 1.2$ mm and $w = 0.03$ mm; (b) a network of the same fibers generated with no exclusion condition $d_{\min} = 0$. In both cases, fiber angles sampled from the distribution (46) with $a_1 = 1$.

angular distribution function, and so we see a convergence of $\langle C_{11}^{e} \rangle$ to $\langle S_{11}^{n} \rangle^{-1}$ as δ increases, accompanied by a convergence of $\langle C_{22}^{e} \rangle$ to $\langle S_{22}^{n} \rangle^{-1}$, to the respective, macroscopic values C_{11}^{eff} and C_{22}^{eff}. It is noteworthy that the lower bound displays a stronger scale dependence; it needs to go up much more than the upper one needs to come down. Due to the connectivity of the stiff (i.e. more conducting) phase, the situation is akin to the case of a matrix with soft disks of Fig. 4 and the case of a matrix with soft needles of Fig. 15. We conclude that, on the macroscale, these two problems are closer to the uniform strain assumption than to the uniform stress assumption. This is opposite to the case of stiff

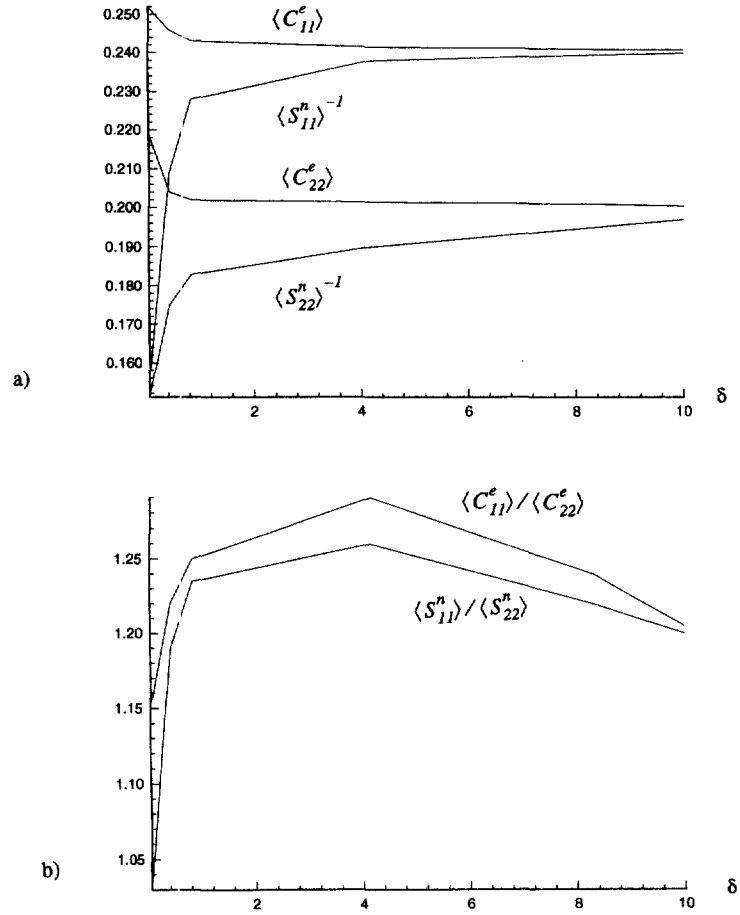

Fig. 17. (a) Hierarchies of bounds, normalized by $C^{\text{fiber}} = 1.0$, for the fiber systems of Fig. 16(a) showing convergence of $\langle C^e_{11}\rangle$ to $\langle S^n_{11}\rangle^{-1}$, and $\langle C^e_{22}\rangle$ to $\langle S^n_{22}\rangle^{-1}$ with increasing δ; $C^{\text{void}} = 0.2$; (b) dependence of anisotropies $\langle C^e_{11}\rangle/\langle C^e_{22}\rangle$ and $\langle S^n_{11}\rangle/\langle S^n_{22}\rangle$ on the mesoscale $\delta = L/\langle l\rangle$.

inclusions in a matrix (Fig. 3), where the response was found to be closer to one resulting from the uniform stress approximation because of the connectivity of the soft phase.

One more natural question to ask here is this: what is the difference, if any, in the effective anisotropy of the composite material based on the essential and natural boundary conditions? We see from Fig. 17(b), which shows both $\langle C^e_{11}\rangle/\langle C^e_{22}\rangle$ and $\langle S^n_{11}\rangle/\langle S^n_{22}\rangle$ as functions of δ, that these anisotropies are different, but tend to converge as δ goes to infinity. This figure exemplifies a fact, also found for some other materials, that the essential boundary conditions lead to a stronger anisotropy than the natural ones.

8. CONCLUSIONS

(1) For any realization of a disordered composite with piecewise-constant realizations, two bounds are available at a point: $\mathbf{C}^e_\delta$ and $\mathbf{S}^n_\delta$, wherein $\delta \equiv L/d$ is the scale of a window of resolution relative to the size of a heterogeneity. This window plays the role of a statistical volume element (SVE). The approach to a deterministic RVE as a function of δ for a material with stiff inclusions is definitely faster than for a material with soft inclusions. Due to the connectivity of the soft matrix, the first case is closer to a state of uniform stress, whereas the second, given the connectivity of the hard matrix, to that of uniform strain.

(2) A calculation involving both types of boundary conditions, essential and natural, avoids unnaturally modifying the material (as it needs to be done using the periodic boundary conditions), while at the same time providing two rigorous bounds on $\mathbf{C}^{\text{eff}}$ for whatever δ. The choice of δ corresponds directly to the amount of computational effort

involved, so that, the more extensive is the computational time and effort, the closer are the bounds on $\mathbf{C}^{\text{eff}}$.

(3) It follows from point 1 that two continuum random fields $\{\mathbf{C}^{\text{e}}_{\delta}(\mathbf{x}, \omega)\}$ and $\{\mathbf{S}^{\text{n}}_{\delta}(\mathbf{x}, \omega)\}$ bound the global, macroscopic response of the random material. On the meso-scale a locally isotropic, inhomogeneous, smooth medium does not exist.

(4) The beta distribution may describe without truncation a wide range of traces of the effective stiffness tensor of composites. When truncation is acceptable, one may use such distributions as Chi, Gumbel-max, Rayleigh, Gauss.

(5) For composites described by stationary and isotropic statistics, the spatial dependence of the correlation function on meso-scale is quasi-isotropic, whereby an elliptical one offers the simplest practical model. This function becomes isotropic when a simultaneous rotation of the coordinate system, in which the meso-scale properties are being measured is implied.

(6) The cross-correlation structure of the crack density (fabric) tensor with the effective response tensors $\mathbf{C}^{\text{e}}_{\delta}$ and $\mathbf{S}^{\text{n}}_{\delta}$ requires further investigation. For needle systems, this correlation is antisymmetric.

Acknowledgements—This research was supported by the NSF under grant no. MSS 9202772.

REFERENCES

Alzebdeh, K. and Ostoja-Starzewski, M. (1993) Micromechanically based stochastic finite elements. *Finite Element Analysis and Design* **15,** 35–41.

Alzebdeh, K. and Ostoja-Starzewski, M. (1996) Micromechanically based stochastic finite elements: length scales and anisotropy. *Probabilistic Engineering Mechanics* **11,** 205–214.

Beran, M. (1968) *Statistical Continuum Theories*. Wiley, New York.

Bird, M. D. and Steele, C. R. (1992) A solution procedure for Laplace's equation on multiply connected circular domains. *Journal of Applied Mechanics* **59**(2), 398–404.

Brenner, C. E. (1991) Stochastic finite elements (literature review). Internal Working Report 35–91, Institute of Engineering Mechanics, University of Innsbruck.

Budiansky, B. and O'Connell, R. J. (1976) Elastic moduli of a cracked solid. *International Journal of Solids and Structures* **12,** 81–97.

Cardy, J. L. (ed.) (1988) *Finite-Size Scaling*. North-Holland, Amsterdam.

Carvalho, F. C. S. and Labuz, J. F. (1966) Experiments on effective elastic modulus of two-dimensional solids with cracks and holes. *International Journal of Solids and Structures* **33**(28), 4119–4130.

Deodatis, G. and Graham, L. (1996) The weighted integral method and the variability response functions as part of SFEM formulation. In *Uncertainty Modeling in Stability, Vibration and Control of Structural Systems*. World Scientific.

Drugan, W. J. and Willis, J. R. (1996) A micromechanics-based nonlocal constitutive equation and estimates of representative volume element size for elastic composites. *Journal of the Mechanics and Physics of Solids* **44,** 497–524.

Frangopol, D. M. and Grigoriu, M. D. (eds) (1996) *Probabilistic Mechanics and Structural Reliability*, ASCE.

Ghanem, R. and Spanos, P. D. (1991) *Stochastic Finite Elements: A Spectral Approach*. Springer, Berlin.

Hazanov, S. and Huet, C. (1994) Order relationships for boundary conditions effect in heterogeneous bodies smaller than the representative volume. *Journal of the Mechanics and Physics of Solids* **41,** 1995–2011.

Hill, R. (1963) Elastic properties of reinforced solids: Some theoretical principles. *Journal of Mechanics and Physics of Solids* **11,** 357–372.

Huet, C. (1990) Application of variational concepts to size effects in elastic heterogeneous bodies. *Journal of the Mechanics and Physics of Solids* **38,** 813–841.

Huet, C. (1991) Hierarchies and bounds for size effects in heterogeneous bodies. In *Continuum Models and Discrete Systems*, ed. G. A. Maugin, Vol. 2. Longman Scientific and Technical, pp. 127–134.

Huet, C. (1994) Experimental characterization, micromechanical simulation and spatio-stochastic approach of concrete behaviours below the representative volume. *PROBAMAT—Probabilities and Materials: Tests, Models and Applications*, ed. D. Breysse, Proc. NATO Adv. Res. Workshop Series E: **269**. Kluwer, The Netherlands, pp. 241–260.

Kachanov, M. (1993) Elastic solids with many cracks and related problems. *Advances in Applied Mechanics* **30,** 259–445.

Kleiber, M. and Hien, T. D. (1993) *The Stochastic Finite Element Method*. Wiley, New York.

Lemaitre, J. and Chaboche, J.-L. (1994) *Mechanics of Solid Materials*. Cambridge University Press, Cambridge.

Mark, R. E. and Gillis, P. G. (1983) Mechanical properties of fibers. In *Handbook of Physical and Mechanical Testing of Paper and Paperboard*, ed. R. E. Mark, Vol. 1. Marcel Dekker, New York, pp. 409–495.

Ostoja-Starzewski, M. (1993a) Micromechanics as a basis of random elastic continuum approximations. *Probabilistic Engineering Mechanics* **8**(2), 107–114.

Ostoja-Starzewski, M. (1993b) Micromechanics as a basis of stochastic finite elements and differences—an overview. *Applied Mechanics Reviews* (Special Issue: Mechanics Pan-America 1993) **46**(11, Pt. 2), S136–S147.

Ostoja-Starzewski, M. (1994) Micromechanics as a basis of continuum random fields. *Applied Mechanics Review* (Special Issue: Micromechanics of Random Media) **47**(1, Pt. 2), S221–S230.

Ostoja-Starzewski, M. and Schulte, J. (1996) Bounding off effective thermal conductivities of multiscale materials by essential and natural boundary conditions. *Physical Review B* **54**(1), 278–285.

Ostoja-Starzewski, M., Jasiuk, I., Wang, W. and Alzebdeh, K. (1996) Composites with functionally graded interfaces: meso-continuum concept and effective properties. *Acta Materialia* **44**(5), 2057–2066.

Ostoja-Starzewski, M., Sheng, P. Y. and Alzebdeh, K. (1996) Spring network models in elasticity and fracture of composites and polycrystals. *Computational Materials Science* **7**(1, 2), 82–93.

Ostoja-Starzewski, M. and Wang, C. (1989) Linear elasticity of planar Delaunay networks: random field characterization of effective moduli. *Acta Mechanica* **80,** 61–80.

Sab, K. (1992) On the homogenization and the simulation of random materials. *European Journal of Mechanics A/Solids* **11,** 585–607.

Sobczyk, K. (1985) *Stochastic Wave Propagation.* Elsevier—PWN.

Stoyan, D., Kendall, W. S. and Mecke, J. (1987) *Stochastic Geometry and its Applications.* Wiley, New York.

Torquato, S. (1991) Random heterogeneous media: microstructure and improved bounds on effective properties. *Applied Mechanics Review* **44,** 37–76.

Vakulenko, A. A. and Kachanov, M. L. (1971) Continuum model of medium with cracks (in Russian). *Mechanics of Solids* **4,** 54–59.

Vanmarcke, E. H. (1983) *Random Fields: Analysis and Synthesis.* MIT Press, Cambridge, MA.

Willis, J. R. (1981) Variational and related methods for the overall properties of composites. *Advances in Applied Mechanics* **21,** 1–78.

Yaglom, A. M. (1957) Some classes of random fields in n-dimensional space, related to stationary random processes. *Theory Probability Applications* **11,** 273–320.